Super-resolution Reconstruction of Orientation Distribution
Function from Motion Scattered Diffusion Weighted Image Slices
and its Application to Fetal Brain Connectivity Study

Xi Cheng

A dissertation submitted in partial fulfillment of the
requirements for the degree of

Master of Science

University of Washington

2015

Reading Committee:

Dr. Colin Studholme, Chair

Dr. Chun Yuan

Dr. Paul Kinahan

Program Authorized to Offer Degree:
Bioengineering

University of Washington

Abstract

Super-resolution Reconstruction of Orientation Distribution Function from Motion
Scattered Diffusion Weighted Image Slices and its Application to Fetal Brain Connectivity
Study

Xi Cheng

Chair of the Supervisory Committee:
Professor Dr. Colin Studholme
Department of Pediatrics, Bioengineering and Radiology

Diffusion-weighted MRI brings new and complimentary information about the development of the brain. It is also actively investigated how diffusion contrast properties correlates with brain diseases. Though promising, this technique faces a number of technical challenges, especially in fetal imaging, where unrestricted movement occurs. Despite the usage of fast imaging sequences, the acquired images are still corrupted by motion artifacts, making them hardly ready to use by doctors or researchers. Therefore, post image processing methods are in great need to estimate the movement of the subject and to reconstruct high quality diffusion volumes for both clinical and research purposes, e.g., the study of fetal brain connectivity.

This thesis firstly gives a background of diffusion and its mathematical models, diffusion inside the brain and diffusion-weighted MRI. Then it introduces the source of the motion artifacts in fetal MRI, and presents the current state-of-the-art method for its removal. After that, a novel super-resolution reconstruction framework for recovering a higher order ODF volume from motion scattered DWI image slices is proposed and experimentally compared to the methods reported in the literature. Both human adult data and macaque fetal data are used for evaluation. Finally, a structural connectivity study of the developing macaque

fetal brains is carried out using unbiased template free brain parcellation schemes and graph theory based analysis.

TABLE OF CONTENTS

Page

ii

LIST OF FIGURES

ACKNOWLEDGMENTS

I wish to thank all those who participated in this work and gave me help and support during my graduate studies.

I would like to express my deepest gratitude to my advisor, Dr. Colin Studholme, for his excellent guidance, caring, and providing me with an excellent atmosphere for my research in his lab, Biomedical Image Computing Group (BICG). Dr. Colin Studholme is a great advisor that teaches me how to be productive and innovative in research. I would also like to thank my supervisory committee members, Dr. Chun Yuan and Dr. Paul Kinahan, for guiding my research and helping me to build my knowledge in medical imaging. Also thanks to Dr. Ruikang Wang, Dr. Ying Zheng and Dr. Michael Bailey for their guidance and help during my research rotations, qualifying exam and pre-general exam.

I would like to show my special thanks to our lab collaborator Dr. Chris Kroenke from Oregon Health and Science University, for providing the macaque data and his patient explanation to my questions related to brain anatomy. I would also like to thank Dr. Francois Rousseau from UMR CNRS/ULP in France for his great advice on my research. Also thanks to Doctor Teresa Chapman in Seattle Children's Hospital for her data and clinical support.

Great thanks to Dr. Sharmishtaa Seshamani and Dr. Mads Fogtmann for their patient research guidance when I was a novice in the lab. Many thanks to other members who are or were in BICG, Jakob Wilm, Mengyuan Liu, Dr. Anna Blazejewska, Dr. Sinchai Tsao, Averi Kisch and Snigdha Kanuparthy for their help in the lab. I would also like to thank my good friends Zheng Li and Dr. Zhongwei Zhi, who are always willing to help me.

Finally, I must thank my family, my parents Min Yang and Shunli Cheng for their support and love with no reservations.

Chapter 1

OVERVIEW

1.1 Background and Motivation

In recent years, there is increased research on diffusion-weighted Magnetic Resonance Imaging (DW-MRI) to study both brain injury and brain growth. It provides an opportunity not only for improved clinical research but also for basic neuroscience studies. [36, 24, 30, 23, 57, 16] Although there has been a significant body of work on the brain studies for adults and babies, applying DW-MRI on in-utero brain studies remains challenging. This is because the uncontrollable fetal motion can severely corrupt the acquired images. Therefore, how to effectively remove the motion artifacts and recover the uncorrupted diffusion volume have constantly attracted attention. The recent development of methods to address fetal motion in conventional structural MRI has led to the first large scale studies of tissue growth and cortical folding in utero. [48, 50, 49] The development of comparable techniques for DW-MRI promises to enable similar advances in the study of structural connectivity development in the developing fetal brain.

1.2 Objective and Contribution

The objective of this thesis are to develop more advanced method for diffusion volume reconstruction from fetal brain DW-MRI, as well as to study how the fetal brain structural connectivity develops. There are two main contributions in this thesis. The 1st one is the development of a robust super-resolution framework for higher order orientation distribution function (ODF) reconstruction from motion scattered DWI slices, presented in Chapter 4. The 2nd contribution is the structural connectivity study for the developing macaque fetal brains using template-free parcellation schemes and small world graph analysis, presented in

Chapter 5.

1.3 Organization

This thesis is structured with 6 chapters aiming to clearly explaining the content it contains.

- Chapter 1: This chapter presents the background, motivation, objectives and contributions of this thesis.

- Chapter 2: This chapter gives a background of diffusion and its mathematical models, diffusion inside the brain and the principle of DW-MRI.

- Chapter 3: This chapter introduces the motion artifacts in fetal brain MRI, and discusses the methodology for motion estimation of DW-MRI.

- Chapter 4: This chapter presents a novel super-resolution framework for robustly reconstructing a higher order ODF volume from motion scattered DWI slices. Experimental results are presented and discussed.

- Chapter 5: This chapter presents the connectivity study for the developing fetal macaque brain using template free parcellation schemes and small world graph analysis.

- Chapter 6: This chapter summarizes this thesis.

Chapter 2

DIFFUSION WEIGHTED IMAGING

This chapter aims to provide an introduction to the physics of diffusion, its typical mathematical models, diffusion inside the brain and the principles of diffusion-weighted MRI.

2.1 Principles of Diffusion

From the atomistic point of view, diffusion is considered as a result of the random walk of the diffusing particles. [40] In molecular diffusion, the moving molecules are self-propelled by thermal energy, which is known as Brownian motion. The concept of diffusion is typically applied to any subject matter involving random walks in ensembles of individuals. The diffusion process is different from bulk motion, where a collection of particles move in a same direction under the influence of an external force. Instead, in the diffusion process each particle moves in its own direction, and collisions happen frequently among particles as a result.

2.1.1 Modelling Diffusion

The diffusion profile can be modeled in several mathematical ways, from simple to complex. In this section, we present the two most common diffusion models, i.e., rank-2 tensor model and spherical harmonic model.

Rank-2 Tensor Model

Rank-2 tensor model is the most widely used diffusion model. It allows to describe anisotropic diffusion, which means that the diffusion can occur at different rates depending on the directions. The directions are typically assumed orthogonal in space, and are usually called

principle directions. The rank-2 tensor has a symmetric form:

$$D = \begin{bmatrix} D_{xx} & D_{xy} & D_{xz} \\ D_{xy} & D_{yy} & D_{yz} \\ D_{xz} & D_{yz} & D_{zz} \end{bmatrix} \tag{2.1}$$

By eigenvalue decomposition, D has the following form:

$$D = [v_1, v_2, v_3] \begin{bmatrix} \lambda_1 & 0 & 0 \\ 0 & \lambda_2 & 0 \\ 0 & 0 & \lambda_3 \end{bmatrix} [v_1, v_2, v_3]^T \tag{2.2}$$

where v_1, v_2, v_3 are the eigenvectors as well as the principle directions, and $\lambda_1, \lambda_2, \lambda_3$ are eigenvalues as well as the diffusion strength or the diffusivities along the principle directions. The symmetric nature of D leaves it with six degrees of freedom. In addition, D is positive symmetric definite (PSD) as the eigenvalues must be positive (or strictly non-negative) due to the physical constraint. Graphically, rank-2 tensor has an ellipsoid profile. Fig. 2.1 illustrates a few rank-2 tensors in their ellipsoid profiles associated with their matrix forms. The diffusion strength along an arbitrary direction g can be retrieved by tensor projection:

$$D(g) = g^T \mathbf{W} g \tag{2.3}$$

There are a number of metrics that can be directly obtained from the rank-2 tensor model, in a form of combining the eigenvalues. [2] Here we list a few mostly common seen metrics, of which Apparent Diffusion Constant (ADC) is defined as:

$$\text{ADC} = \frac{\lambda_1 + \lambda_2 + \lambda_3}{3} \tag{2.4}$$

It is straightforward that the ADC metric measures the overall diffusion strength along the three principal diffusion directions.

The Fractional Anisotropy (FA) metric is defined as:

$$\text{FA} = \sqrt{\frac{(\lambda_1 - \lambda_2)^2 + (\lambda_2 - \lambda_3)^2 + (\lambda_3 - \lambda_1)^2}{2(\lambda_1^2 + \lambda_2^2 + \lambda_3^2)}} \tag{2.5}$$

$$\begin{bmatrix} 1 & 0 & 0 \\ 0 & 1 & 0 \\ 0 & 0 & 1 \end{bmatrix} \quad \begin{bmatrix} \frac{1}{2} & 0 & 0 \\ 0 & 2 & 0 \\ 0 & 0 & 1 \end{bmatrix} \quad \begin{bmatrix} 3 & 0 & 0 \\ 0 & \frac{1}{3} & 0 \\ 0 & 0 & 1 \end{bmatrix} \quad \begin{bmatrix} 1 & \frac{1}{2} & 0 \\ \frac{1}{2} & 1 & 0 \\ 0 & 0 & 1 \end{bmatrix}$$
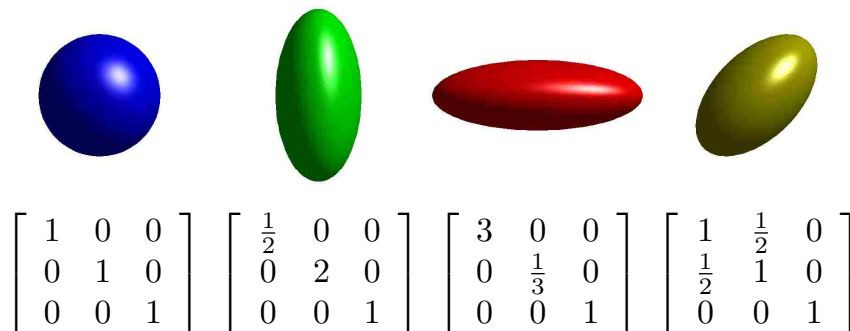
Figure 2.1: Examples of rank-2 tensor profiles in the 1st row and their associated matrix forms in the 2nd row.

The FA metric measures the anisotropic property of the diffusion profile. It has a smallest value of 0 for isotropic diffusion (i.e., $\lambda_1 = \lambda_2 = \lambda_3$), and a highest value of 1 if the diffusion takes place along only one principle direction (i.e., only one λ is non-zero). Therefore, the FA value always varies between 0 to 1. The higher the FA value is, the more anisotropic the diffusion is.

The rank-2 tensor model is sufficient in many application situations, however, its limitation should be kept in mind. That is, the rank-2 tensor model can only model diffusion with an ellipsoid profile, which is unfortunately too simple to model complex diffusion profiles. Examples are shown in Fig. 2.2, where the non-ellipsoid profiles on the left can only be approximated by rank-2 tensors on the right. From the figure, we find that if a diffusion profile have more than one diffusion directions, the rank-2 tensor is unfortunately not able to capture that information. This will inevitably cause problems in some applications, i.e., how to distinguish crossing white matter tracts inside the brain, which is discussed in chapter 4.

Spherical Harmonic Model

To overcome the limitation of the rank-2 tensor model, spherical harmonic model is employed. It consists of an infinite summation of real spherical harmonic (SH) basis functions of different
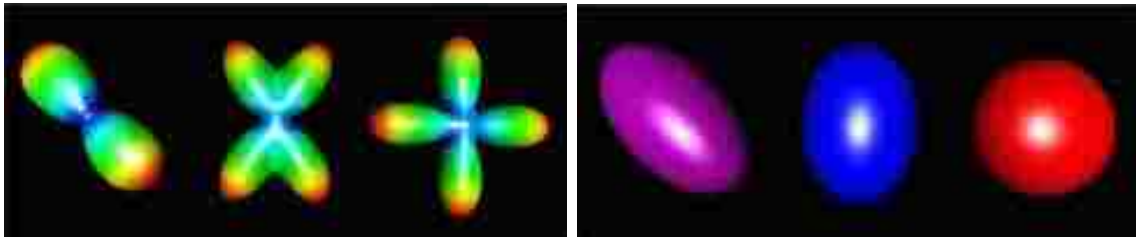
Figure 2.2: Examples of non-ellipsoid profiles on the left are approximated by the rank-2 tensors on the right..

degrees. The diffusion strength along a direction g is computed by

$$D(g) = \sum_{l=0}^{\infty} \sum_{m=-l}^{l} w_l^m Y_l^m(\theta, \phi) \tag{2.6}$$

where Y_l^m the real spherical harmonics basis functions with degree l and order m. θ and ϕ are the angles in the angular coordinate system, which can be easily converted from g. The profiles of some lower degree basis functions ($l = 0, 1, 2, 3$) are shown in Fig. 2.3 for better understanding. With the spherical harmonic model, any arbitrary diffusion profile can be described. However, computational complexity increases dramatically as with the degree of the basis functions, therefore a reasonable upper limit for the degree number should be properly chosen for practical applications. In addition, it is clear from the figure that only basis functions with even degrees are antipodal symmetrical. Since the diffusion is antipodal symmetric, only the spherical harmonic basis functions of even degrees should be employed for modeling, i.e., l should be kept even.

2.1.2 Diffusion inside the Brain

The diffusion is not free therefore anisotropic inside the brain. An important factor for anisotropic water diffusion is the hindrance of perpendicular water diffusion by the myelin sheath encasing the axons. The numerous lipid bilayers of myelin have limited permeability to water and are expected to hinder diffusion across the fibres, particularly the axonal water,
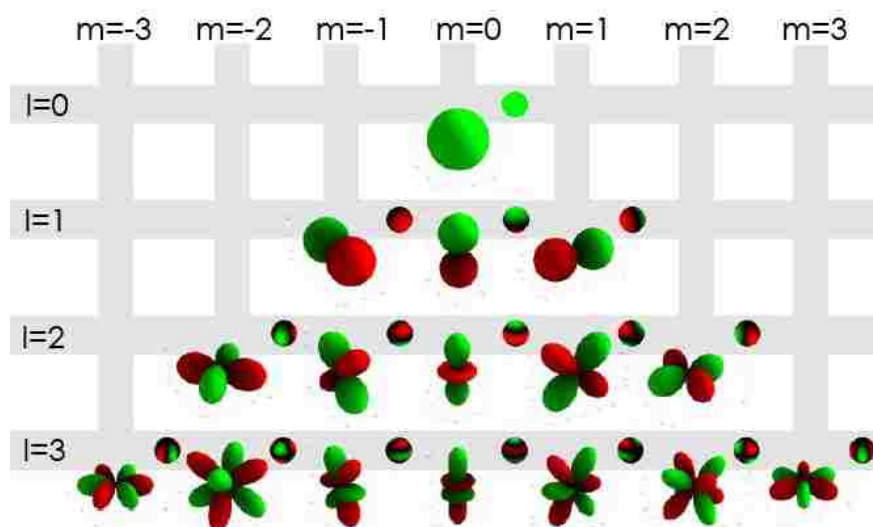
Figure 2.3: Visualization of the profiles of the spherical harmonic basis functions of degree from $l = 0$ to $l = 3$. Modified figure from [14], released into the public domain.

relative to the length of the axons where such barriers do not exist.[4, 5] It is also important to keep in mind that a lot of other factors other than myelination can lead to diffusion anisotropy inside the brain, such as cell membranes.

Diffusion MRI imaging happens at resolutions on the order of millimeters. The greatly exceeds the size of neural structures which is on the order of microns. The aim of diffusion imaging is therefore to image a microscopic process that occurs in micro-structures. This causes inaccuracy if the micro-structures are not well ordered. However, we are lucky that the brain is a highly ordered, in the sense that thousand of axons are running along each other to form fiber tracts inside the white matter.

2.2 Diffusion Weighted MRI

Diffusion weighted imaging (DWI) is a form of imaging based upon measuring the random Brownian motion of water molecules within a voxel of tissue. [21] It emerges as a valuable imaging modality to characterize the white-matter microstructure [30, 54, 8]. Particularly,

the information gathered by DWI has lead to great progress in the human connectome project. [9] This comprises a complete description of neuronal connectivity in the brain, which promises to greatly expand our knowledge about the brain.

2.2.1   The MRI Experiments

MRI experiments all rely on the application of a strong magnetic field of strength B_0, which aligns the magnetic spins of all atoms inside the scanner. In relaxation contrast MRI imaging, the tissue dependent proton density (PD), rate constant T_1 and T_2 determine the signal amplitude. The degree to which T_1 and T_2 influence the image contrast is determined by the repetition time (TR), which is the time between two consecutive excitations, and the echo time (TE), which is the time after spin excitation where peak signal intensity occurs. For details of MRI, a good reference is [20].

Diffusion weighting is a method in MRI experiment allowing the amount of diffusion to be reflected in the imaging contrast. The basic principle behind diffusion weighting is the application of a dephasing gradient followed by a rephasing gradient. [1] The process of dephasing and rephasing have no effect on stationary spins. However, for spins that move along the applied gradient direction, their effects cannot be cancelled out. This results in a smaller contribution to signal intensity for water molecules that diffuse. In other words, diffusion leads to a weakened intensity in the acquired images.

A scan in the DW-MRI experiment consists of a measurement S_0 without diffusion weighting, and several measurements S_g with diffusion weighting but along different directions g.

2.2.2   The Stejskal-Tanner Equation

The measurements S_0 and S_g are linked via the well-known Stejskal-Tanner(ST) equation [47]

$$\ln(\frac{S_g}{S_0}) = -bD(g) \tag{2.7}$$

where $D(g)$ is the diffusion strength along direction g. The parameter b, which is the so-called *b-value*, is a collection of a number of MRI experiment related parameters, e.g., the gyromagnetic ration, the strength of the gradient and so on. In practical DW-MRI experiments, people always choose an appropriate b-value and ignore the factors it is composed of. For example, a value of $b = 500s/mm^2$ is used in the fetal macque scans whose data is used in the experiments presented in the following chapters. Typically, higher b-value indicates more diffusion weighing and therefore higher accuracy for ODF reconstruction than lower b-values. However, high b-value also requires long diffusion time which results in a longer echo time and further a lower Signal to Noise Ratio (SNR) of the acquired images. Therefore, an appropriate b-value needs to be carefully chosen as a trade-off between different aspects of the acquired images.

2.2.3 Determination of the Rank-2 Tensor

Given sufficient measurements of diffusion strength along different directions, any kind of diffusion profile mentioned above can be estimated with high accuracy. We present the process of estimating the rank-2 tensor model as an example. Because there are six degrees of freedom in the rank-2 tensor, at least 6 diffusion measurements along non-collinear diffusion directions are needed, in addition to S_0. While 6 measurements are the least, employing more diffusion directions for MRI experiments makes the tensor estimation more accurate.

We generalize Eqn. 2.7 to the rank-2 order tensor model, as in Eqn. 2.8.

$$\ln(\frac{S}{S_0}) = -bgDg^T \tag{2.8}$$

Assuming in total N non-collinear diffusion directions are employed for measurements, the diffusion tensor can be estimated via least square fitting, as in Eqn. 2.9.

$$
\begin{bmatrix} D_{xx} \\ D_{yy} \\ D_{zz} \\ D_{xy} \\ D_{xz} \\ D_{yz} \end{bmatrix} = \begin{bmatrix} g_{1,x}^2 & g_{1,y}^2 & g_{1,z}^2 & g_{1,x}g_{1,y} & g_{1,x}g_{1,z} & 2g_{1,y}g_{1,z} \\ g_{2,x}^2 & g_{2,y}^2 & g_{2,z}^2 & g_{2,x}g_{2,y} & g_{2,x}g_{2,z} & 2g_{2,y}g_{2,z} \\ \vdots & \vdots & \vdots & \vdots & \vdots & \vdots \\ g_{N,x}^2 & g_{N,y}^2 & g_{N,z}^2 & g_{N,x}g_{N,y} & g_{N,x}g_{N,z} & 2g_{N,y}g_{N,z} \end{bmatrix}^{-1} \begin{bmatrix} \ln\frac{S_1}{S_0} \\ \ln\frac{S_2}{S_0} \\ \vdots \\ \ln\frac{S_N}{S_0} \end{bmatrix} \tag{2.9}
$$

The whole DW-MRI experiment finally gives us one image volume without diffusion weighting and N image volumes with different diffusion weighting. If these image volumes are aligned perfectly well during the scan, Eqn. 2.9 is carried out per voxel for tensor estimation. However, if there are motion artifacts, this per-voxel fitting process becomes inaccurate. How to estimate the motion to reposition the voxels to where they should be, and perform the subsequent ODF reconstruction from the scattered data are the focuses of the next two chapters, i.e., chapter 3 and chapter 4.

Chapter 3

MOTION ESTIMATION FOR DWI SLICES

3.1 Introduction

As mentioned in the previous chapter, the estimation of a diffusion profile is based on a set of diffusion measurements and a non-diffusion measurement for a same place. If the subject moves, the set of measurements are scattered in the space. In order to build the correspondence of these measurements, movement of the subject needs to be known or estimated. Therefore, motion correction is crucial for reconstruct all the diffusion profiles in the domain.

Fetal MRI is a particularly challenging task, as the fetal brain moves with a large extend within highly deformable maternal tissue, resulting in highly corrupted images. If using a fast echo planar imaging (EPI) acquisition, it is a common assumption that the within-slice motion can be ignored for most cases. However, motion between slice excitation causes the slice sets scattered in the space. As illustrated in Fig. 3.1(a), the fetal brain moves when the slices are acquired. If we consider these slices parallel to each other with respect to the brain anatomy as how they are physically acquired, the resulting image is corrupted known as motion artifacts, as illustrated in Fig. 3.1(b). To recover the underlying anatomy, it is necessary to estimate the changes in position and orientation of the DWI slices and reposition them accordingly with respect to the underlying anatomy, as shown in Fig. 3.1(c).

The motion extension in fetal MRI is usually larger than that in adult MRI due to the lack of subject cooperation and the less restriction of the motion in in-utero. In addition, maternal breathing introduces another kind of motion. As an example, Fig. 3.2 shows a macaque brain image from three different views. The scan was performed on the coronal plan of the brain. From the figure, we can see that the coronal view (the 3rd row) has almost no motion artifact, which confirms the assumption that within-slice motion can be ignored.
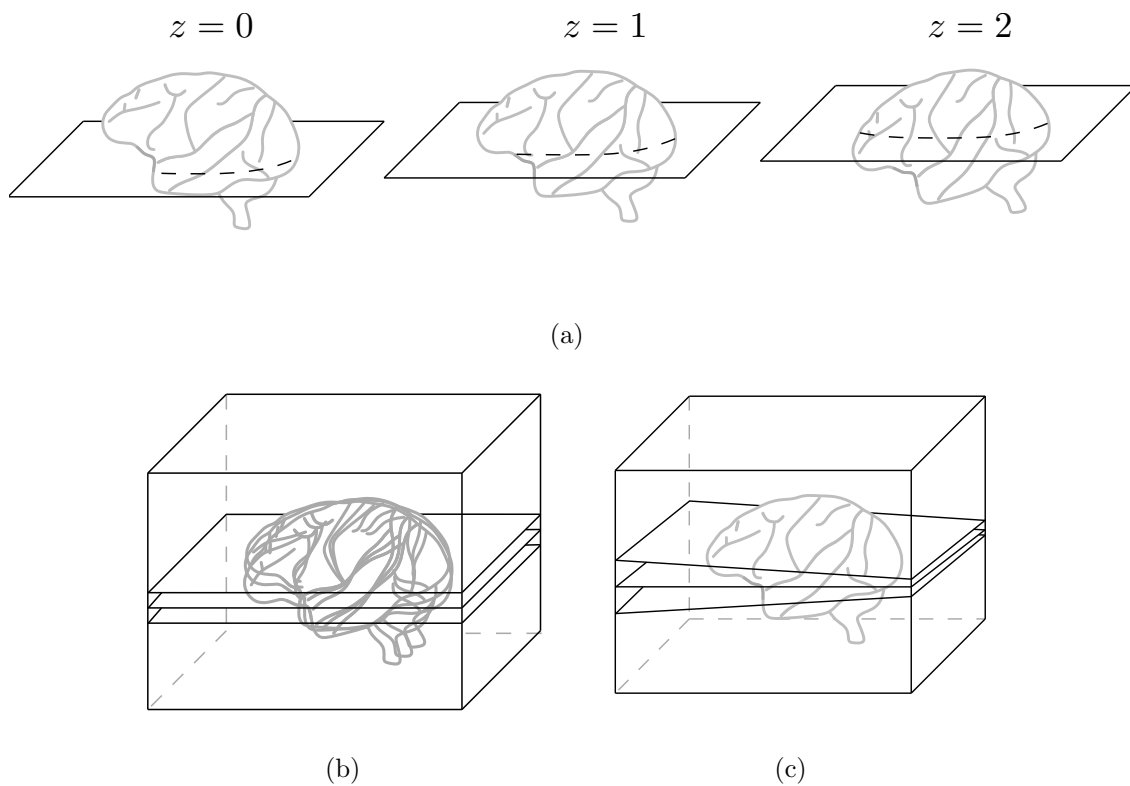
Figure 3.1: (a) The subject (brain) is moving during the scan. (b) If no motion estimation is performed, the acquired slices are considered parallel to each other, resulting in image artifacts. (c) Motion artifacts can be removed by repositioning the slices, known as motion correction. Modified figure from [56].
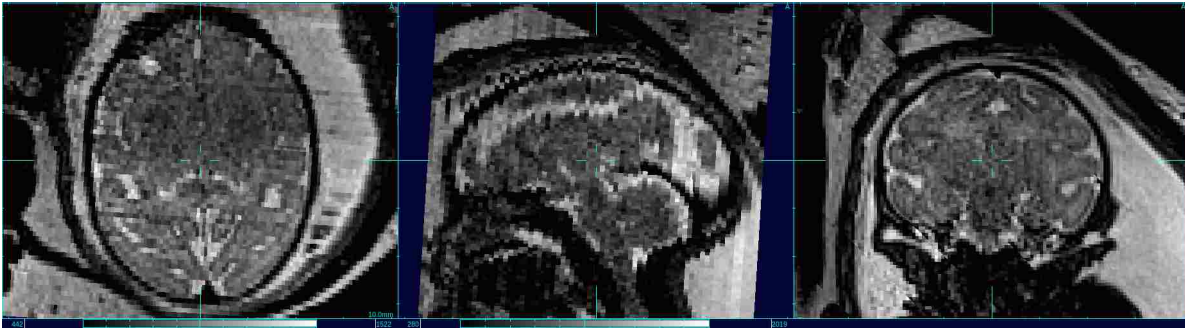
Figure 3.2: A structural image from a fetal macaque brain, shown in three orthogonal views. The motion artifacts due to maternal breathing are clear in the image. Note that the coronal view has no artifacts because that is the 2D place in which the slices are acquired.

However, the axial and saggital views are corrupted due to the between-slice motion. Note that the motion artifact in the image is primary due to maternal breathing as the subject was sedated during the scan.

There have been a number of published works for fetal motion correction for different kinds of MRI, e.g., structural MRI [41, 28, 32, 17, 12], functional MRI [31, 38, 46] and DW-MRI [27, 32, 37, 13]. Compared to motion correction fro structural MRI and fMRI data, DW-MRI data is more challenging because of the physical relationship of the measurements, modeled by the ST equation. Up till [13], all the work for DW-MRI motion correction simply ignores modeling this relationship and treats the DW-MRI as the structural MRI. While this simplification can remove the artifacts to some extend, better results can certainly be achieved if the relationship is incorporated in the algorithm design. In the method section, we briefly introduce the current state-of-the-art methodology for DW-MRI slice motion estimation as in [13].

3.2 Methods

3.2.1 DW Slice Motion Estimation Framework

In this section, we present the approach for estimating rigid motion parameters for all the slices, denoted as Φ, assuming that the ground-truth diffusion volume I is given. To estimate Φ, we want to maximize its probability. That is:

$$\underset{\Phi}{\mathrm{argmax}}\ p(\Phi|S, I) = \underset{\Phi}{\mathrm{argmax}}\ p(S|I, \Phi)p(\Phi|I) \tag{3.1}$$

where S is the set of slices and $\Phi = \{\phi_k\}_{k=1}^{K}$ is the set of to-be-estimate slice motion transformations. By assuming statistical independence of the measurement noise between acquired slices and the independence between the reconstructed volume I and motion transformations Φ, we convert problem (3.1) to

$$\underset{\Phi}{\mathrm{argmax}}\ p(\Phi|S, I) = \underset{\Phi}{\mathrm{argmax}}\ p(\Phi) \prod_{k=1}^{N} p(S_k|I, \phi_k) \tag{3.2}$$

where $p(S_k|I, \phi_k)$ is the likelihood function for each acquired slice. By further assuming the statistical independence of the measurement noise over all the voxels $x's$ in slice S_k, the likelihood can be estimated from a generative model

$$p(S_k = s_k|I, \phi_k) = \prod_{x} exp(-\gamma(x)\|s_k(x) - E[S_k|I, \phi_k](x)\|_{L_2}^2) \tag{3.3}$$

where $\gamma(\cdot)$ is a binary function approximately selecting the collection of voxels under rigid motion, which is the brain in this application. The expected value for each voxel in a 2-D slice, i.e., $E[S_k|I, \phi^k](x)$ can be estimated by locating the 2-D slice in the 3-D diffusion volume I given its transformation. We defer its discussion to section 4.2.3.

3.2.2 Motion Prior

The motion of fetal brain can be modeled as a succession of random rigid transformations, which consist of 3 translation parameters and 3 rotation parameters. Since the interleaving

slices have timing information which can be obtained from the DICOM data files, they can be temporally reordered.

The term $p(\Phi)$ allows us to incorporate prior knowledge on the slice motion due to the brain movement into the optimization. The regularization form should be:

$$p(\Phi) = \prod_k \exp(-\beta \cdot d(\phi_k, \phi_{k+1})) \tag{3.4}$$

where β is a constant controlling the regularization strength, and d measures the distance between the transformations for adjacent slices.

As mentioned above, ϕ is rigid transformation parameter that contains 6 elements. If assuming it obeys the Gaussian distribution, and putting equal emphasize between translation and rotation parameters, we can define the distance between the transformations using L_2 norm as:

$$d(\phi_k, \phi_{k+1}) = \| \phi_k - \phi_{k+1} \|_{L_2}^2 \tag{3.5}$$

An observation from the data is that, the fetal head motion is generally smooth but with some large abrupt changes among the intervals of the slice acquisitions. Therefore, the assumption of Gaussian distribution and the subsequent $L2$ norm metric may not be accurate for modeling. Instead, the Huber norm is a better choice to be applied here, The Huber function is a combination of L_1 norm and L_2 norm, which is defined as:

$$L_\delta(a) = \begin{cases} \frac{1}{2}a^2, & \text{for } |\, a\, | \le \delta. \\ \delta(|\, a\, | - \frac{\delta}{2}), & \text{otherwise.} \end{cases} \tag{3.6}$$

Then, we can write $p(\Phi)$ as:

$$p(\Phi) = \prod_k \exp(-\beta \| \phi_k - \phi_{k+1} \|_{L_\delta}^2) \tag{3.7}$$

Finally, we plug equations (3.3) and (3.7) into equation (3.2), and take the logarithm of it. This leads to the complete formula that estimate Φ.

$$\hat{\Phi} = \operatorname*{argmin}_{\Phi} \sum_{k=1}^{K} \sum_{x \in S_k} \gamma(x) \| s_k(x) - E[S_k|I, \phi_k](x) \|_{L_2}^2 + \beta \sum_{k=1}^{N-1} \| \phi_k - \phi_{k+1} \|_{L_\delta}^2 \tag{3.8}$$

3.2.3 Link to ODF Volume Reconstruction

In the DWI slice motion estimation framework, we assume that the ground-truth ODF volume I is given, which allows the incorporation of ST equation to the relate diffusion and non-diffusion weighted signals. This is also indicated in Eqn. 3.1. However, this assumption can hardly be valid as I is also what we want to estimate. This gives us an chicken-and-egg situation, where the motion parameters Φ is needed for estimating the ODF volume I, meanwhile I is needed for the determination of Φ as well. In the regime of optimization, this situation can be disentangled by alternately estimating one parameter set, i.e., Φ or I, while freezing the other parameter set, i.e., I or Φ. The alternating process leads to a convergence for both of the sub-optimization problems, and therefore enable a good estimation of both parameter sets. We discuss the details of ODF volume (I) reconstruction in Chapter 4.

Chapter 4

SUPER-RESOLUTION ODF RECONSTRUCTION FROM MOTION SCATTERED DWI SLICES

4.1 Introduction

The previous chapter has discussed about how to remove motion artifacts for DW-MRI due to the subject movement. As a result of the motion, the acquired 2-D slices are no longer regular sampled and the orientations of the DW slices are no longer consistent with the diffusion measurement directions during the scan, as in Fig. 4.1(a). In other words, when the estimated transformations from motion correction process are applied to map the acquired slices into a consistent anatomical frame, measurements are scattered in both spatial and angular domains. It is a necessity to formulate a continuous 3-D ODF volume as in Fig. 4.1(b) from these motion scattered slices. The 3-D diffusion volume is then used for subsequent image processing like tractography. The ODF volume can be considered as a 3-D volume of which each voxel contains an ODF rather than a single value. To achieve this, techniques for estimating the ODF onto the regularly sampled voxel grid are needed. This is the focus of this chapter.

Jiang [27] described the first work on fetal slice motion correction using an interpolation method to fit a rank-2 tensor diffusion model to the observed slice data. Oubel [37] suggested a model free interpolation approach to reconstruct a 5-D regularly sampled diffusion volume. Interestingly this may permit fitting of more complex diffusion models than the rank-2 tensor. In this approach, a 5-D spatio-angular radial basis function (RBF) interpolation was employed to account for motion effects in both the diffusion location and diffusion direction spaces. However, the approach is limited because the relation between the diffusion directions in the angular space, modelled by the ST equation, can not be well approximated
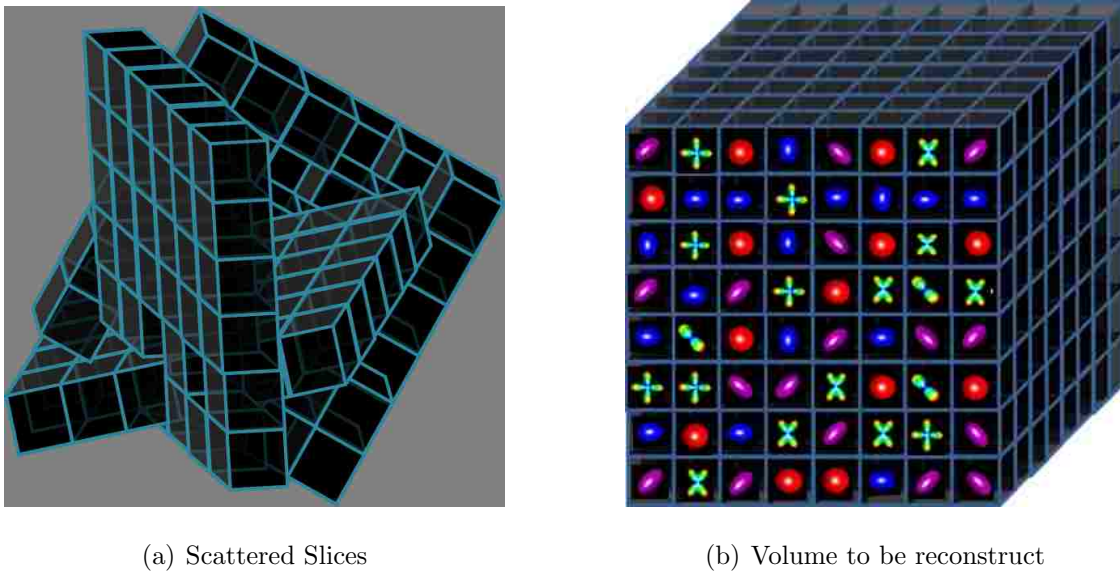
(a) Scattered Slices   (b) Volume to be reconstruct

Figure 4.1: (a) 2-D imaging slices become scattered in the space after being repositioned using their estimated geometric transformations. (b) An ODF volume of higher resolution can be reconstructed from the scattered DWI slices.

by the proposed angular RBF.

A key limitation of these interpolation based methods is that they cannot incorporate spatial deconvolution of multiple acquisitions to enhance the resolution of the final model. Conventional fetal MRI studies in particular make extensive use of multi-slice acqusitions with fine in-plane resolution in multiple thick slice planes to provide views with complimentary resolution [41] . These multiple views can be exploited by fusion to form a single image with both enhanced signal to noise and enhanced resolution [42]. In diffusion imaging of adults, Scherrer [44] proposed a method to perform super resolution (SR) reconstruction from orthogonal anisotropic DW acquisitions, where no motion occured between slices, by estimating a sequence of 3-D volumes for all the diffusion measurement directions. To make the diffusion directions consistent for each acquisition, Kriging was used for interpolation in angular space, which could introduce errors in this domain. Recently, Fogtmann [13] proposed a novel unified framework for both diffusion direction sensitive slice registration and

iterative 3-D DTI reconstruction from moving brain anatomy. This used a single measure of mismatch between the rank 2 diffusion model being estimated and observed slices to refine both slice alignment and deconvolution by alternating between solving these two problems. For reconstruction, the maximum a posterior (MAP) method enables explicit modelling the slice resolution to generate SR reconstruction from multiple slice orientations. Though this framework has been proved to be a significant improvement compared to the previous work, it focuses on the simple rank-2 tensor model for alignment. For the final reconstructed image, this limits its application when describing voxels containing crossing fibers, a condition referred to as intravoxel orientational heterogeneity (IVOH) [37]. In conventional DWI where no motion scattering occurs, a significant body of work has shown the ability of higher order models to better represent the underlying anatomy [45, 52]. However, these works do not directly extend to slice scattered data or incorporate spatial deconvolution to provide isotropic resolutions from multiple sets of thick slices with acquired with different orientations.

In this chapter, we summarize the published ODF reconstruction frameworks, and propose a method to robustly reconstruct a higher order ODF model at isotropic spatial resolutions from motion scattered DW-MRI slices. Experimental comparison is further made. Specifically, we extend iterative reconstruction approaches to a spherical harmonic (SH) model and estimate the coefficient parameters at each voxel based on a maximum likelihood framework. This model fitting incorporates an explicit slice profile deconvolution allowing isotropic spatial SR reconstruction of the diffusion model on a regular voxel lattice.

4.2   Methods

4.2.1   Scattered Multi-slice DW Data

We focus on single shot, multi-slice echo planar spin echo imaging to provide optimum robustness to within-slice motion. The sequence collects a stack of $N + 1$ regularly sampled images $\tilde{S} = \{\tilde{S}_0, \tilde{S}_1, \ldots, \tilde{S}_N\}$, where $\tilde{S}_0$ denotes data obtained without diffusion weighting, and $\tilde{S}_{i=1:N}$ denotes DW images acquired with diffusion-sensitizing direction g_i in the fixed

scanner coordinate system and strength b. Ideally, $\tilde{S}_0$ and $\tilde{S}_i$ are related through the ST equation, i.e., $\tilde{S}_i = \tilde{S}_0 e^{-bD_i}$, where D_i is the diffusion strength along direction g_i. However, distortions due to fetal motion within the scanner coordinate frame destroy this relationship by scattering the measurements in space. In this work we assume that slice registration has retrieved the spatial transformation parameters mapping the data into a consistent anatomical frame. Again the within-slice motion is ignored. We express the original data $\tilde{S}$ in the unit of a slice, i.e.$\tilde{S} = \{S_i\}_{k=1}^K$. Each slice S_i is associated with its spatial mapping X_i and diffusion-sensitizing direction g_i, which can represent where this slice sensitivity lies in the fixed coordinate system. In the case of rigid body between-slice motion, denoted as ϕ^k, which consists of a rotation R and translation T, each slice is transformed to a location $\{X_i', g_i'\}$ by $X_i' = R_i X_i + T_i$ and $g_i' = R_i g_i$ in the anatomical frame.

4.2.2 Super-resolution Reconstruction Framework

Super-resolution (SR) is a large research field encompassing many applications. [53, 25] In our application, the principle of SR is to combine low resolution (LR) images to produce an image that has a higher spatial resolution than the original images. For MRI data of subjects under motion control, the SR work mainly focuses on using lower resolution data acquired on a regular grid and often assuming simple translation between the lower resolution sample grids. [19, 39, 7] In comparison, the fetal brain MRI data which consists of multiple 2-D thick slices is more challenging, as it is corrupted by full 3-D rigid motion on a slice by slice basis. Though this data specificity does not affect the way that the SR problem is modelled, it introduces additional challenges because SR becomes a reconstruction problem with scattered anisotropic data.

As in most of common SR approaches, we model the problem in our application according to its physical observation and then estimate a solution by inverting this model: [42]

$$s_k = M_k B_k \phi_k I + n_k \quad \text{for} \quad 1 \le k \le K \tag{4.1}$$

where I is the high resolution (HR) ODF volume, s_k denotes the k-th LR image slice. M_k is a

subsampling matrix, B_k is a blur matrix, ϕ is the geometric transformation of k-th LR image slice. n represents the noise. K is the number of slices of the LR images. The purpose of SR is to remove the effect of the blurring convolution and to increase the voxel grid density.

The unknown ODF volume I is estimated by inverse the observation model:

$$\hat{\mathbf{I}} = \underset{\mathbf{I}}{\operatorname{argmin}} \sum_{k=1}^{K} \|s_k - M_k B_k \phi_k I\|_{L_2}^2 \tag{4.2}$$

The L_2 norm is used here because we assume that the image noise n follows a Gaussian distribution. Solving Eqn. 4.2 is an ill-posed problem, which means that the solution $\hat{\mathbf{I}}$ cannot be uniquely determined. In this regard, some form of regularization plays a key role and must be included in the energy function to stabilize the problem or constrain the space of solutions. [51] This leads to

$$\hat{\mathbf{I}} = \underset{\mathbf{I}}{\operatorname{argmin}} \sum_{k=1}^{K} \|s_k - M_k B_k \phi_k I\|_{L_2}^2 + \alpha \cdot \operatorname{Reg}(I) \tag{4.3}$$

where α is a constant controlling the regularization strength.

4.2.3 Simulate LR Images using Observation Model

As in the observation model, we can synthesize the 2-D LR image slice following $M_k B_k \phi_k I$. In our application, it has the following expression as in 4.4:

$$M_k B_k \phi_k I(x) = \int G(z) S_0(\phi_k(x+z)) e^{-bD(I(x+z), \phi_k(x+z), g_k')} dz \tag{4.4}$$

The 3-D Gaussian kernel $G(z)$ is used for modelling the in-plane point spread function (PSF), which corresponds to the blurring effect by M_k. Still, ϕ_k represents the geometric transformation effect. Due to the scattering nature of the data, $\phi_k(x+z)$ is often not lying on 3-D regular grid of the reconstructed volume. The downsampling effect is implicitly encoded here. To get the value at these specific locations, tri-linear interpolation on the grid is used. $D(\cdot)$ is where the diffusion model plugs in, which can be both rank-2 tensor model or spherical harmonica model. For spherical harmonic model based experiments in
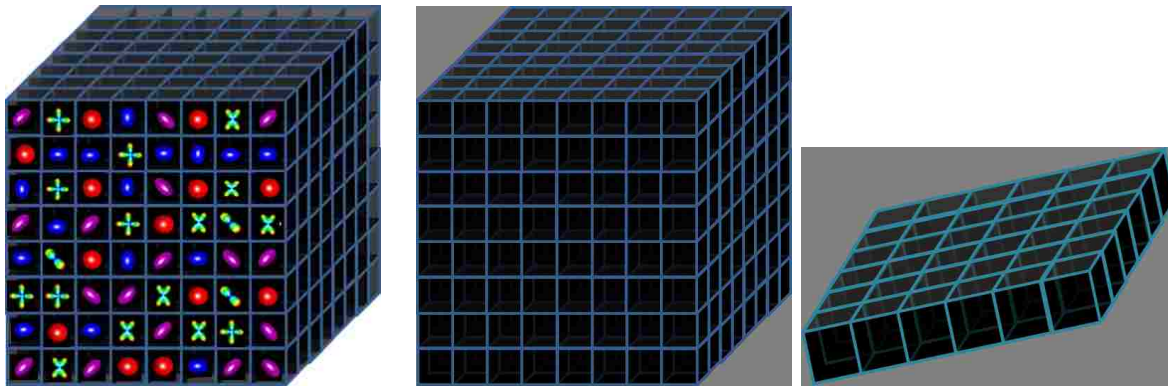
(a) A 3-D ODF volume to be reconstruct

(b) A 3-D volume of single diffusion values

(c) A 2-D slice of single diffusion values

Figure 4.2: The steps of simulating a 2-D slice. A 3-D ODF volume (a) firstly gets projected along a specific diffusion direction. This results in a 3-D volume of single diffusion values (b), which is further projected to a 2-D slice of single diffusion values (c).

the following sections, the spherical harmonic basis functions of the first three even degrees, i.e., $l = 0, 2, 4$ are used, making the total number of the spherical harmonic basis functions to be 15.

In equation 4.4, ST equation is explicitly incorporated as $S_0(\phi_k(x+z))e^{-bD(I(x+z),\phi_k(x+z),g'_k)}$. This term consists of two projections. The first one is in the spherical domain, from the ODF to a single diffusion value along a specific direction. From this projection, we get a 3-D volume of single values as in Fig. 4.2(b) from a 3-D volume of ODFs as in Fig. 4.2(b), which is just I. The 3-D volume of single values is further projected to a 2-D slice as in Fig. 4.2(c), given the geometrical transformation.

4.2.4 Image Regularization

Image regularization allows us to incorporate prior knowledge on the reconstructed volume into the optimization. Most medical image reconstruction applications assumes some kind of spatial homogeneity by using metrics such as smoothness [44] or total variation [29].

Specifically, we want to encourage I to be piecewise smooth permitting abrupt changes at boundaries between uniform regions of tissue. This can be achieved by using the Huber norm and setting

$$\text{Reg}(I) = \sum_{x,g \in I} \| \bigtriangledown_{x,g} I(x,g) \|^2_{L_\delta} \tag{4.5}$$

$\bigtriangledown$ is chosen as the first order discrete gradient operator. The SH coefficients are treated equally, which means that we apply the same regularization on each of the 3-D SH coefficient maps. Finally, the whole objective function is given in equation 4.6 and is optimized by any standard gradient based optimization method. L-BFGS method is used in this work.

$$\hat{\mathbf{I}} = \underset{\mathbf{I}}{\arg\min} \sum_{k=1}^{K} \| s_k - M_k B_k \phi_k I \|^2_{L_2} + \alpha \cdot \sum_{x,g \in I} \| \bigtriangledown_{x,g} I(x,g) \|^2_{L_\delta} \tag{4.6}$$

4.2.5   Link to Maximum Log-likelihood

The principle behind the super-resolution reconstruction framework is maximum log-likelihood. That is, we want to maximize the probability of the unknown 3-D HR image volume I given all the 2-D LR image slices and their geometric transformations. Applying the maximum a posterior (MAP) framework, we can write it as:

$$\underset{I}{\arg\max}\, p(I|S, \Phi) = \underset{I}{\arg\max}\, p(S|I, \Phi) p(I|\Phi) \tag{4.7}$$

where S is the set of slices and $\Phi = \{\phi^k\}_{k=1}^{K}$ is the set of estimated slice geometric transformations. By assuming statistical independence of the measurement noise between acquired slices and the independence between the reconstructed volume I and motion transformations Φ, we convert problem (4.7) to

$$\underset{I}{\arg\max}\, p(I|S, \Phi) = \underset{I}{\arg\max}\, p(I) \prod_{k=1}^{N} p(S_k|I, \phi_k) \tag{4.8}$$

where $p(S_k|I, \phi^k)$ is the likelihood function for each acquired slice. By further assuming the statistical independence of the measurement noise over all the voxels $x's$ in slice S_k, the likelihood can be estimated from a generative model where s_k has a mean value of $E[S_k|I, \phi_k]$. It

follows a distribution corresponding to L. For example, a Gaussian distribution corresponds to L_2 norm. It has the following form:

$$p(S_k = s_k | I, \phi_k) = \prod_x \exp(-\|s_k(x) - E[S_k|I,\phi_k](x))\|_L^2 \tag{4.9}$$

$E[S_k|I,\phi_k]$ has the same form as in equation (4.4).

The image prior $p(I)$ assumes that the image gradient, both spatially or spherically, follows a distribution with a mean value of 0. If this distribution is assumed to be corresponding to the Huber norm, we can write $p(I)$ as:

$$p(I) = \prod_{x,g} \exp(-\alpha \parallel \bigtriangledown_{x,g} I(x,g) \parallel_{L_\delta}^2) \tag{4.10}$$

If we plug equations (4.9) and(4.10) into equation (4.8) and take the logarithm of it, we get the exactly same equation (4.6), which is the super-resolution reconstruction framework.

4.3   Imaging Data

4.3.1   Human data

This set of DW-MRI data was acquired from an adult male volunteer using a Siemens 3T Trio scanner using a single shot EPI sequence with 20 noncollinear diffusion gradient measurement directions with imaging parameters b=1000s/mm^2, TE=94ms and TR=10900ms. This has a voxel resolution of $1.885 \times 1.885 \times 2$mm^3 and significant signal to noise ration in comparison to abdominal fetal DWI data. There are 3 stacks in total, with motion artifact only present in the third stack.

4.3.2   Macaque data

This set of DW-MRI data was acquired from a sedated macaque fetus *in utero* at gestational age 135 days (of a total gestational term of 165 days) using a Siemens 3T Trio scanner at the Oregon National Primate Research Center. This scan consists of nine axial, nine coronal, and nine sagittal single shot EPI sequences with eddy current compensation along 20 noncollinear

diffusion gradient directions with b=500s/mm^2, TE=90ms and TR=5000ms. Thus, this scan gives 27 sets of diffusion data in total. The voxel resolution is 1.125×1.125×3mm^3. The primary source of minor motion in this dataset was due to maternal breathing and was corrected using the method in [13].

4.4 Experiments and Results

4.4.1 Rank-2 Tensor Model

To validate the reconstruction using the rank-2 tensor model, we carry out the experiments using the fetal macaque data. We extract the FA map from the reconstructed rank-2 tensor map, and perform tractography to recover fibers crossing corpus callosum using the deterministic Fiber Assignment by Continuous Tracking (FACT) algorithm [35]. The resolution of the reconstructed volume is set to be isotropic 0.75mm for the macaque imaging data. The parameters were set to be $\alpha = 10^8$ and $\delta = 40$. Convergence of the L-BFGS typically required 15 iterations using a gradient tolerance of less than 10^{-6}.

Principal Diffusion Direction Map

We extracted the FA map and principle direction map from the reconstructed rank-2 tensor ODF map via eigenvalue decomposition. We also emphasize relatively more anisotropic diffusion by weighting the principle direction map by the FA map on a voxel by voxel basis. The result for the fetal macaque data is shown in Fig. 4.3.

Tractography

We perform tractography to recover white matter fiber tracts running across the corpus callosum. This is done by manually selecting seeds central to the corpus callosum structure. The recovered tracts are shown in Fig. 4.4, where the structural development of the corpus callosum fiber tract is in accordance with the expectation.
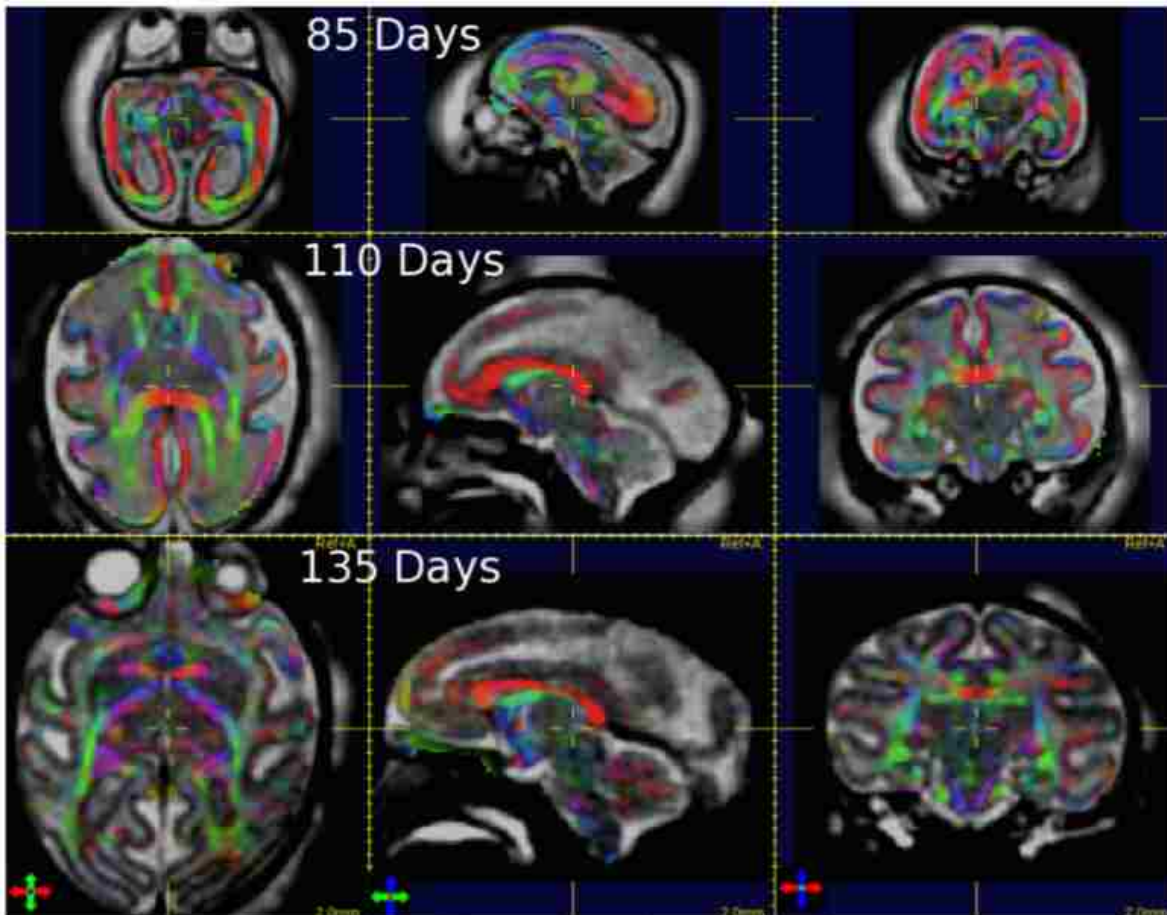
Figure 4.3: Principle diffusion direction map weighted by the FA map on a voxel by voxel basis from a fetal macaque brain, at gestational ages of 85 days, 110 days and 135 days, as indicated in the figure, respectively. The principle directions are color-coded, where red denotes left-right, green denotes front-back and blue denotes top-bottom direction of the brain. We show the views in axial, saggital and coronal planes, as from the leftmost column to the rightmost column of the figure, respectively.
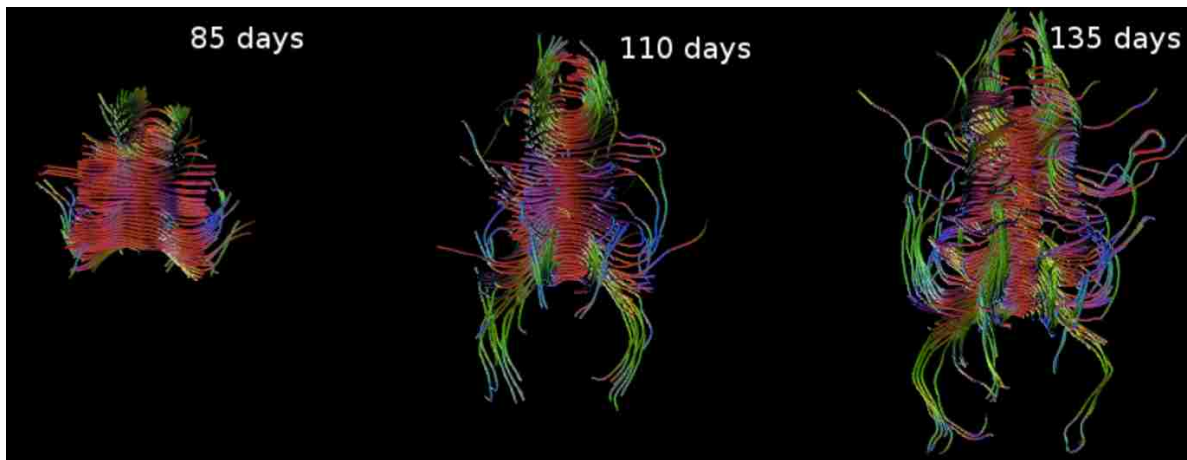
Figure 4.4: White matter fibers running through the corpus callosum from a fetal macaque brain, at gestational ages of 85 days, 110 days and 135 days, as indicated in the figure, respectively. The fiber tracts are color-coded by the directions, where red denotes left-right, green denotes front-back and blue denotes top-bottom direction of the brain.

4.4.2 Spherical Harmonic Model

To validate the reconstruction using the spherical harmonic model and to compare it to the rank-2 tensor model, we first perform reconstruction using both of the models. In both cases, the resolution of the reconstructed volume is set to be isotropic 0.75mm for the fetal macque data and isotropic 0.5mm for the adult human data. The parameters were also set to be $\alpha = 10^8$ and $\delta 40$. Convergence of the L-BFGS typically required 25 iterations using a gradient tolerance of less than 10^{-6}. In observation of different properties of adult human data and fetal macaque data, we design different experiments accordingly as below.

Experiments for Human Adult data

In adult brain, the white matter structure has already fully developed, which the ODF profile can not be simply modeled by the rank-2 tensor in some regions, i.e., where multiple fibers meet together. In terms of the image quality, it has a high SNR, which allow the

reconstruction of a higher order ODF with high accuracy. Therefore, it can be used to validate the correctness of the reconstruction framework.

Visualization of spherical harmonic coefficient maps. Since each spherical harmonic basis function is unique in the orientation and the variation frequency along that orientation it encodes, we firstly directly visualize the coefficient maps for the basis functions. Fig. 4.5 shows the coefficient maps of the spherical harmonic basis functions of degree-0 in column 1, and degree-2 in the following five columns. From the figure, we can see that white matter tracts having a same diffusion direction are reflected in a same coefficient map, and is also in accordance with the orientation encoded in the spherical harmonic basis function.

Direct ODF Visualization. To evaluate the ability of the SH model to detect multiple fiber tracts, we directly visualize and compare ODFs from the two models. To locate voxels which contain multiple fiber tracts, we refer to the FA weighted principle diffusion direction map obtained by the rank-2 tensor model, as shown in Fig. 4.6(a). From the coronal view in Fig. 4.6(a), it is clear that the voxel marked by the white "+" mark is in the region where the corpus callosum and the cortical-spinal tracts meet. Comparing Fig. 4.6(b) and (c), we can see that the spherical harmonic model in (c) successfully depicts the crossing fiber structure which is not achieved by the rank-2 tensor model in (b).

Experiments for Fetal Macaque data

The lack of motion artifacts in the original data allows us to use the reconstructed diffusion as the ground truth to explore slice scattering in the following experiments. Apart from direct ODF visualization, we considered using FA map to interpret and compare the results from the two models. The FA map from a rank-2 tensor diffusion volume is easily obtained by the eigenvalue decomposition. To estimate the FA map from the spherical harmonic diffusion volume, we estimate the diffusion strength along the directions of the eigenvectors obtained from the rank-2 tensor for each voxel.

Reconstruction from Scattered Image Data To simulate the scattered data in a
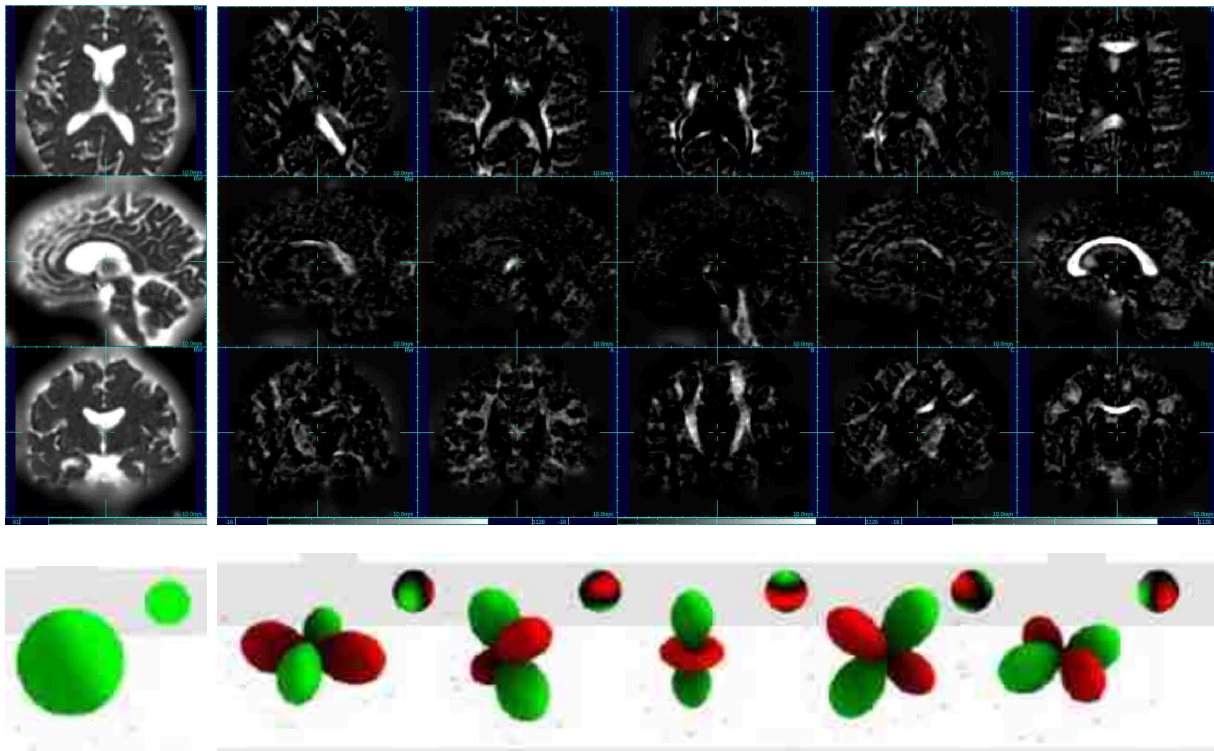
Figure 4.5: The coefficient maps of the SH basis functions of degree-0 in the 1st column and degree-2 in the following five columns. The corresponding profiles of the SH basis functions are shown right below.
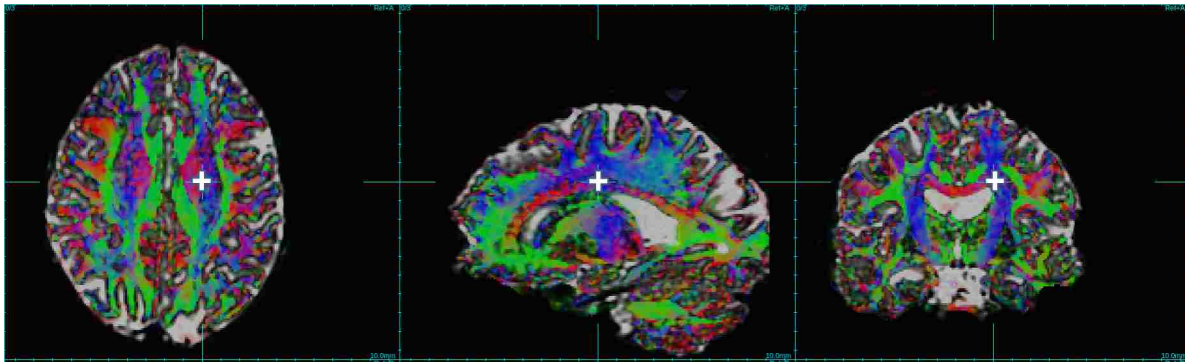
(a)
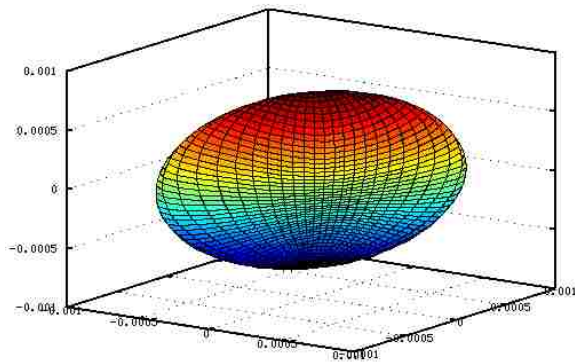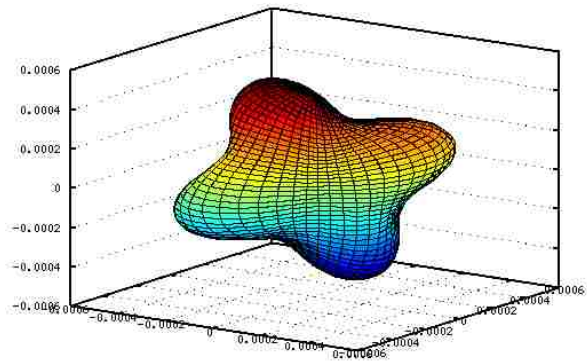
(b)   (c)

Figure 4.6: (a) An voxel lies on the crossing point of the corpus callosum and the cortical-spinal tracts is selected, as indicated by the white "+" mark; (b) diffusion profile described using the rank-2 tensor model; (c) diffusion profile described using the spherical harmonic model.

(a)

(b)
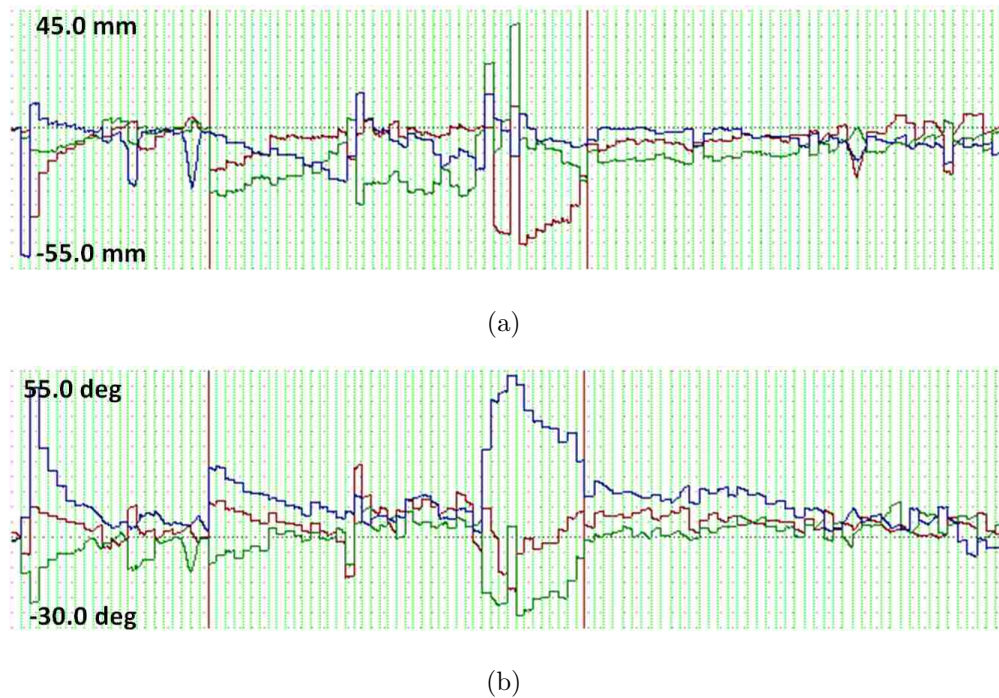
Figure 4.7: The slicewise head motion trajectory for a human fetal brain in a clinical DW scan. (a) translation along X,Y,Z directions in red, green, blue respectively; (b) rotation along X,Y,Z directions in red, green, blue respectively. The long solid vertical lines separate the slices of different planes.

realistic manner, we use the high quality reconstructed primate fetal data and a measured human fetal head motion trajectory from a clinical DW scan. The human study consisted of 2, 4 and 4 copies of axial, saggital and coronal datasets, respectively. Each scan was along 10 noncollinear diffusion gradient directions, giving 2904 data slices in total. This motion trajectory is estimated by a slice registration based technique in [13], and is shown in Fig. (4.7).

Since the primate study contains more slices (11634) than that of the human fetal study (2904), we extend the length of the known motion trajectory by concatenating reflected copies of the human trajectory to create a contiguous time series. This is used to simulate the 27 motion scattered sets of primate data, whose resolution and planar orientation are estimated

to match the original scans. Using the known slice transformations back to a common reference anatomy, we perform the iterative reconstruction using the spherical harmonic model from all the 27 sets of the motion scattered data. The result is then compared to that from the reconstruction using the original non-motion scattered 27 sets of data.

Evaluation of Amount of Data for Reconstruction. In order to simulate a realistic human study with less imaging time, we perform reconstruction using only 12 out of the 27 sets of the motion scattered data, with equal number of sets for axial, coronal and sagittal planes. The FA map and ODF are computed and compared to those obtained using all 27 sets of data.

Experimental Results. The reconstructed FA maps from all the experiments above are shown in Fig. 4.8. Comparing the first two columns, we can see that the SH model recovers the very similar FA volume as the rank-2 tensor model, which validates our method on the non-motion scattered data. The comparison of column 3 to column 2 shows the robustness of our method on the motion scatted data. From the last column we can also conclude that our method is robust to more realistic human fetal studies with less imaging time.

The voxel selected to contain multiple fiber tracts is indicated by the white crossing mark in the first row of Fig. 4.9. It lies on the crossing point of the developing corpus callosum and the cortical-spinal tracts. The reconstructed ODFs from all the experiments above are all shown in Fig. 4.10. From (a) and (b), we can find that the reconstructed ODF from SH model has more power in detecting multiple fiber tracts within a voxel over the rank-2 tensor model. The developing myelinated fibers are illustrated using the blue lines. (c) and (d) validates that our proposed method is robust in the case of motion scattered data and a realistic human fetal study time.

4.5 Discussion and Conclusions

In the chapter, we have presented a framework for robustly reconstructing the ODF model at isotropic spatial resolution from motion scattered DW-MRI slices. We also propose to extend iterative reconstruction approaches to a spherical harmonic (SH) model from the rank
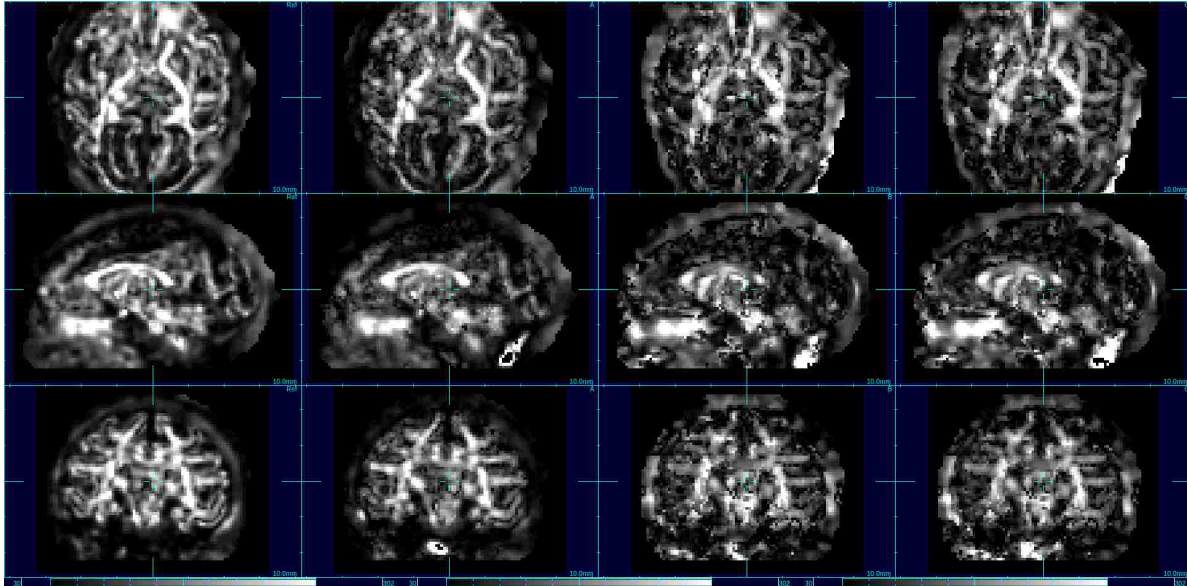
Figure 4.8: Consistency of basic diffusion measures: FA map reconstructed from column 1) rank-2 tensor model using all 27 stacks of original data; 2) SH model using all 27 stacks of original data; 3) SH model using all 27 stacks of simulated motion scattered data; 4) SH model using 12 stacks of simulated motion scattered data. Results are shown in axial, saggital and coronal views from the top to the bottom row, respectively.
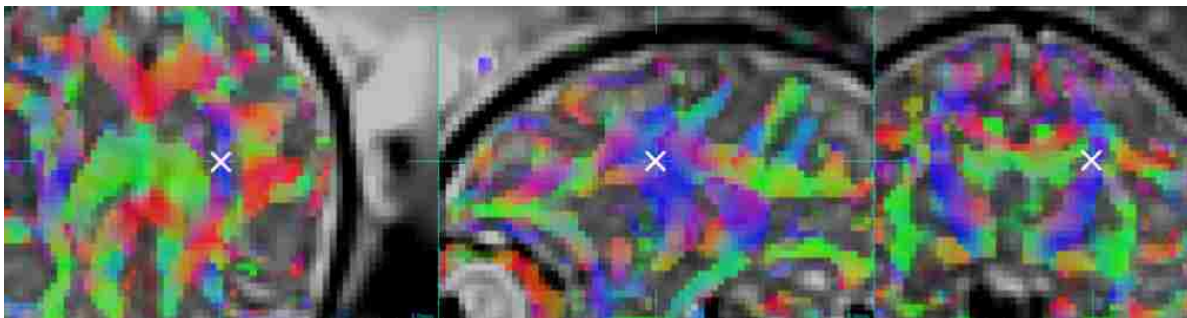
Figure 4.9: The FA weighted principle diffusion direction map in axial, saggital and coronal planes. The white marked voxel contains multiple fiber tracts.

(a)   (b)

(c)   (d)
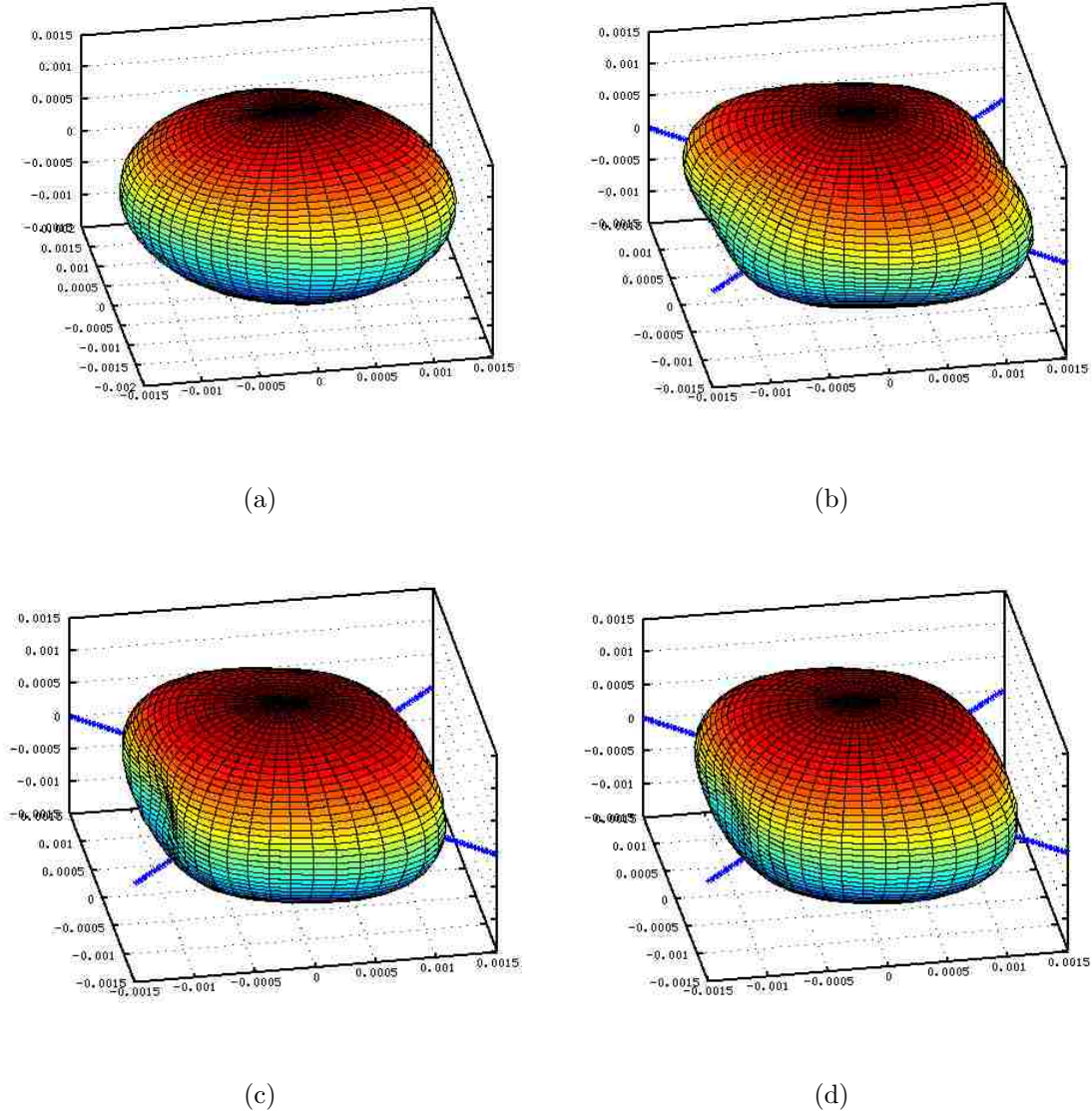
Figure 4.10: The ODFs reconstructed from (a) rank-2 tensor model using all 27 stacks of original data; (b) SH model using all 27 stacks of original data; 3) SH model using all 27 stacks of simulated motion scattered data; 4) SH model using 12 stacks of simulation motion scattered data. The blue lines in (b)-(d) illustrate the developing myelinated fibers. All ODFs are viewed from the same angle and scale.

2 tensor model, which enables crossing fiber detection. The iterative reconstruction fit of the model parameters and spatial deconvolution was achieved using a maximum likelihood framework.

Experiments with both the human adult and fetal primate brain data show that our proposed SH-based approach can correctly recover more complex ODF than the rank-2 tensor model from the motion-scattered slice data in and after later gestational ages, which will make it possible to accurately depict crossing fiber tracts from especially in-utero imaging data.

Chapter 5

STUDY OF FETAL BRAIN CONNECTIVITY IN SERIAL IMAGING STUDIES

5.1 Introduction

The brain can be considered as a network of highly interconnected small regions. Therefore studying its structural connectivity can help provide a better understanding of the organization of the brain. Recently, non-invasive techniques such as diffusion-weighted MRI have been used to study structural connectivity in adults and infants which have led to the discovery of small-world characteristics of the brain [26][18]. More recently, Fan [10] studied the brain network of healthy pediatric subjects at ages of 1 month, 1 year and 2 years, and identified the development of small-world topologies in this early period of development.

A typical pipeline for studying brain connectivity using DW images is shown in Fig. 5.1. Specifically, both DW image and structural image (e.g., T1-weighted or T2-weighted) are acquired for a same subject. Image artifacts such as motion artifacts are carefully removed if there is any. Volume registration is then carried out to align the DW image and the structural image. After that, white matter fiber tracing (i.e., tractography) is performed using the DW image, while brain parcellation into functional regions is carried out using the structural image. With the parcellated regions considered as graph nodes, and their connections as graph edges which are established if there are fibers running between, a connectivity graph for the brain can be assembled. The brain connectivity property can then be examined by standard graph analysis.

An important step in these studies is the partitioning of the brain into functional regions of interest (ROI's) between which connectivity is evaluated. [55, 6] The adult and pediatric brain parcellation schemes focus on dividing the cortex into units that represent known
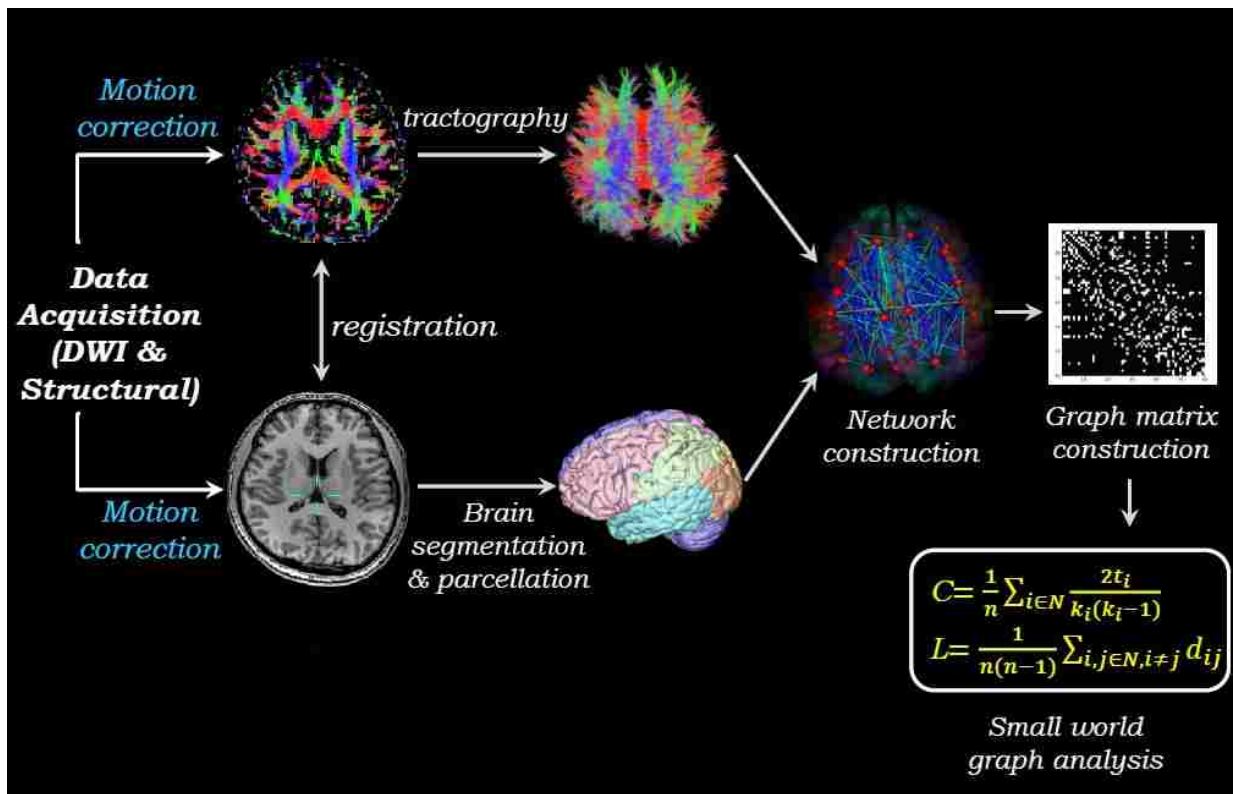
Figure 5.1: A pipeline for the study of brain connectivity using both DW and structural MRI image data.

(a) 85 days   (b) 110 days   (c) 135 days
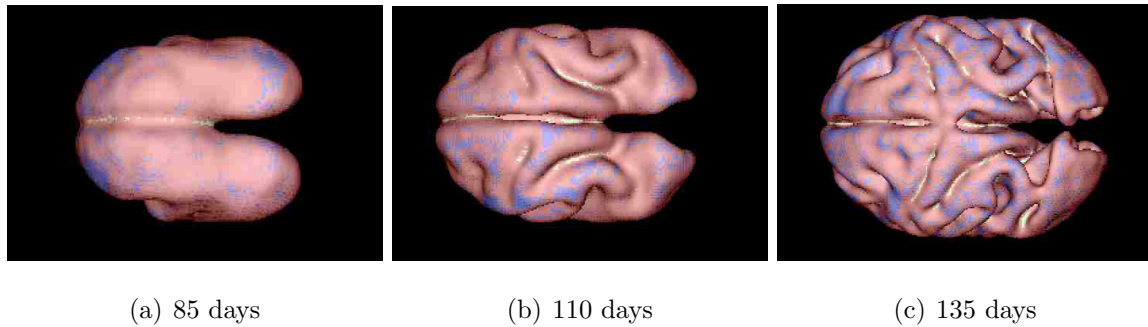
Figure 5.2: The brain of a same macaque fetus but at different gestational ages.

functional divisions often defined in MRI by the presence of cortical folds or sulci and gyri. However in the developing fetal brain such units may not be present at a given gestational age and their structural correlates in the form of sulci and gyri are not developed. An example is shown in Fig. 5.2, where the dramatic change of the shape of a same fetal brain at different gestational ages is clearly shown.

In order to study early brain growth we therefore must develop a connectivity mapping methodology that is independent of cortical folding and its rapid change over time. A very recent structural connectivity study [54] of neonatal brains used two automated methods for parcellating the brain surface, i.e., (1) the brain was partitioned using 3D regular lattice into spatial regions of equal spatial extent along the x, y, and z axes of the imaging volume, and (2) derived subcortical surface was divided based on Recursive Zonal Equal Area Sphere Partition. However, for serial studies of growth over time these approaches create partitions which can have inconsistencies in region areas as the brain grows. The first method may break regions unexpectedly and results in large differences in ROI sizes, especially when the number of ROI's increases. In addition to cortical partitioning, in the fetus we are also interested in dividing the developing cerebral mantle. Unfortunately, the second method which is basically surface projection cannot be applied here. Hagmann [22] used a two phase random parcellation method to study the adult brain structural connectivity. However the number of ROI's cannot be pre-determined in this method. This is a limitation in the case

where one is interested in performing a controlled analysis of network by varying the number of nodes systematically.

Rather that assuming a specific functional and anatomical correspondence over time from which to derive connectivity measures as the brain rapidly develops, here we explore approaches that simply aim to sample that anatomical or functional pattern and its connectivity in a way that allows us to evaluate spatial connectivity as the brain grows. As with any imaging process, sampling of spatial data can be achieved using different schemes. Here we explore adaptations of regular and random sampling with the aim of ensuring consistency of anatomical sampling over time. We use animal imaging data (the macaque monkey) as a basis for this study as it provides a high quality reference not currently available in normal human studies.

5.2 Materials and Methods

5.2.1 Data Acquisition

We acquired a dataset consisting of both T2-weighted and Diffusion Weighted Imaging (DWI) data of an in-vivo monkey fetus at gestational ages of 85, 110 and 135 days from a 3T Siemens scanner. The T2-weighted data consists of 12 scans with a resolution of $0.667 \times 0.667 \times 1mm$, $TE = 97ms$, $TR = 9900ms$. The DWI data consists of 3 scans, each containing 27 stacks (9 axial, 9 sagittal and 9 coronal) with a resolution of $1.125 \times 1.125 \times 3mm$, 20 diffusion weighted directions, $b = 500s/mm^2$, $TE = 93ms$ and $TR = 5000ms$.

5.2.2 Data Preprocessing

The T2-weighted multi-slice acquisitions were motion corrected and reconstructed to isotropic 0.5mm voxels with the approach described in [12]. All the DWI acquisitions were motion corrected and reconstructed to a rank 2 tensor with an isotropic spatial resolution of 0.75mm [13], which was then registered to the reconstructed T2-weighted volume and up-sampled to the same resolution as T2-weighted volume. The T2-weighted image was segmented into

(a) random parcellation

(b) regular parcellation
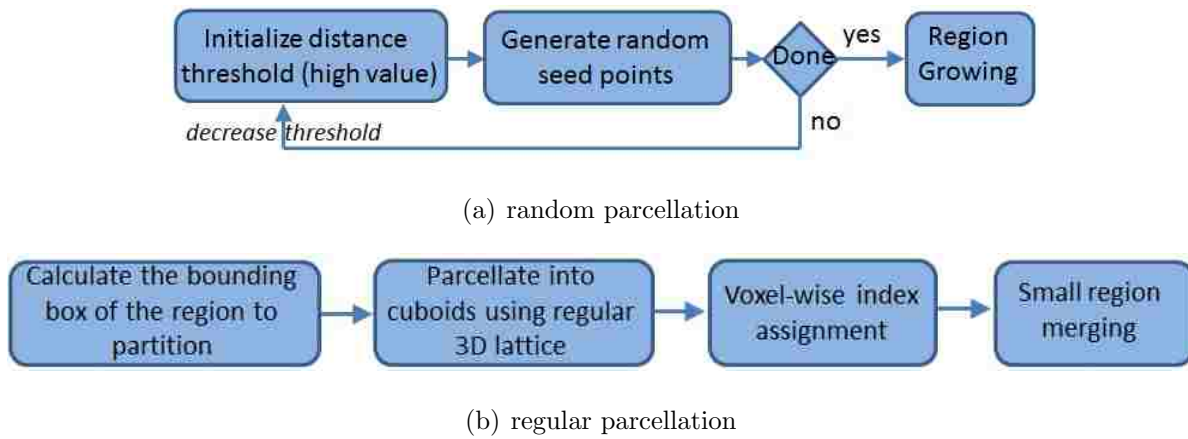
Figure 5.3: Parcellation Algorithm Overview: different steps in (a) random parcellation, and (b) regular parcellation.

two basic regions: the cortical plate and cerebral mantle. The cerebral mantle here included subplate, intermediate zone, deep grey matter and germinal matrix.

5.2.3 Region Partition

We consider 2 types of parcellation schemes whose steps are shown in Fig. 5.3.

Random parcellation

A number of seed points are randomly generated within the mask followed by region growing, where all voxels in the mask are assigned to the nearest seed point. To avoid trivial ROI's whose size would be much lower than that of others, a distance threshold was used to make the random seed points well distributed when they were generated. This ensured that the distance between any pair of seed points was above the threshold. An appropriate threshold is selected by first creating the partitioning with a high value and reducing this until the required number of seed points is generated.

Regular parcellation

All volumes (T2-weighted, DTI and mask) were manually transformed to standardize the axial orientation and centering. A bounding box of the mask was calculated and then divided into cuboids of equal size. These cuboids were then assigned an integer index derived from their x, y, z locations in the image space. The individual image voxels within the brain mask were then assigned label values corresponding to the index of the cuboid they were in. The assignment may result in small boundary ROI's when the mask is irregular, whose connection to other ROI's can be meaningless. Therefore, ROI's whose sizes were smaller than a predefined threshold were merged into its nearest ROI recursively until the sizes of all ROI's were larger than the threshold.

Comparison of Two Parcellation Schemes

Compared to the regular parcellation scheme, the random parcellation scheme has several advantages. In particular, it allows more direct control over the number of ROI's within the brain mask and avoids the creation of trivial ROI's at the brain boundary when the brain shape becomes more complex. For random parcellation, we repeated the experiments 40 times for each number of ROI's to specifically examine the consistency as the sampling of the functional regions is varied. We also varied the number of ROI's in both parcellation schemes to examine its effect on the connectivity measures. Specifically, we partitioned the cerebral mantle into ROI's of which the number varies from 60 to 140 in subcortical connectivity study. In cortical connectivity study, we partitioned the cortical plate into ROI's of which the number ranges from 30 to 65 only using the random parcellation.

5.2.4 Tractography

Whole-brain streamlined fiber tractography was performed with the deterministic Fiber Assignment by Continuous Tracking (FACT) algorithm [35], using a mask consisting of the sub-plate, cortical mantle, deep grey matter and germinal matrix segmented from the re-

constructed T2-weighted volume. A maximum turning angle of 45°, a minimum fractional anisotropy (FA) of 0.08 and a tracing step size of 0.1 voxel were chosen. This step recovers the fiber tracts in the white matter.

5.2.5 Network Graph Analysis

The unweighted connectivity network graph was constructed using the ROI's resulting from the parcellation as nodes. Two nodes are considered connected if there exists at least one fiber connecting them. The unweighed graph is also represented as an binary adjacency matrix $A_{N \times N}$, where N is the number of ROI's and $A_{ij} = 1$ if the i-th and j-th node are connected and 0 otherwise. Small-world analysis was applied to the graph which involved computing measurements of segregation (cluster coefficient) and integration (global efficiency) [43] and comparing these metrics to those of a randomized network with the same number of nodes and degree distribution. The cluster coefficient (C) and global efficiency (E) are defined as :

$$C = \frac{1}{n} \sum_{i \in N} C_i = \frac{1}{n} \sum_{i \in N} \frac{2t_i}{k_i(k_i - 1)} \tag{5.1}$$

$$E = \frac{1}{n} \sum_{i \in N} E_i = \frac{1}{n(n-1)} \sum_{\substack{i,j \in N \\ i \neq j}} \frac{1}{d_{ij}} \tag{5.2}$$

where C_i is the cluster coefficient and k_i is the degree of the node i, t_i is the number of triangles formed by the neighbouring nodes of node i, E_i is the global efficiency of node i, d_{ij} is the number of nodes along the shortest path from node i to node j, n is the total number of nodes in the node set N.

Small-world networks are characterized by dense local clustering of connections between neighbouring nodes and short path lengths between any pair of nodes due to the existence of relatively few long-range connections [3]. Thus, its clustering coefficient is much larger than that of a randomized network ($C >> C_{rand}$), while its global efficiency is slightly smaller ($E < E_{rand}$).

(a) brain network
(b) random network
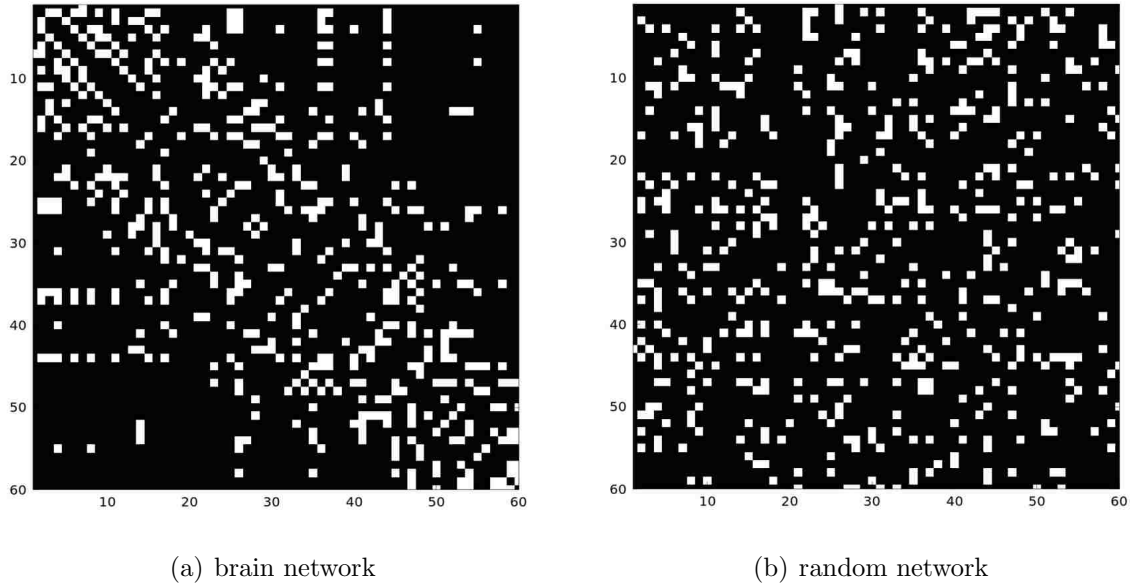
Figure 5.4: Binary adjacency matrices of the brain network and its randomized form containing 60 nodes. White denotes connection while black denotes disconnection.

5.3 Experimental Results

We performed both subcortical and cortical connectivity studies on the acquired data.

Subcortical connectivity

Fig. 5.5 shows an example of partitioning the same brain (cerebral mantle) at all 3 ages using both regular and random parcellation schemes. Fig. 5.6 shows the traced fiber tracts connecting cortical ROI's at all 3 time points, which are colored by the FA map and overlaid on the corresponding T2-weighted images. We then constructed the brain connectivity network graph for each dataset based on the ROI's and all traced fiber tracts.

The binary adjacency matrix of both the brain network and its randomized network were calculated, with an example shown in Fig. 5.4. ROI's were assigned the indices in the order of the distance from their geometric centers to the origin point $(0, 0, 0)$ in the Euclidean

Random partition   Regular partition

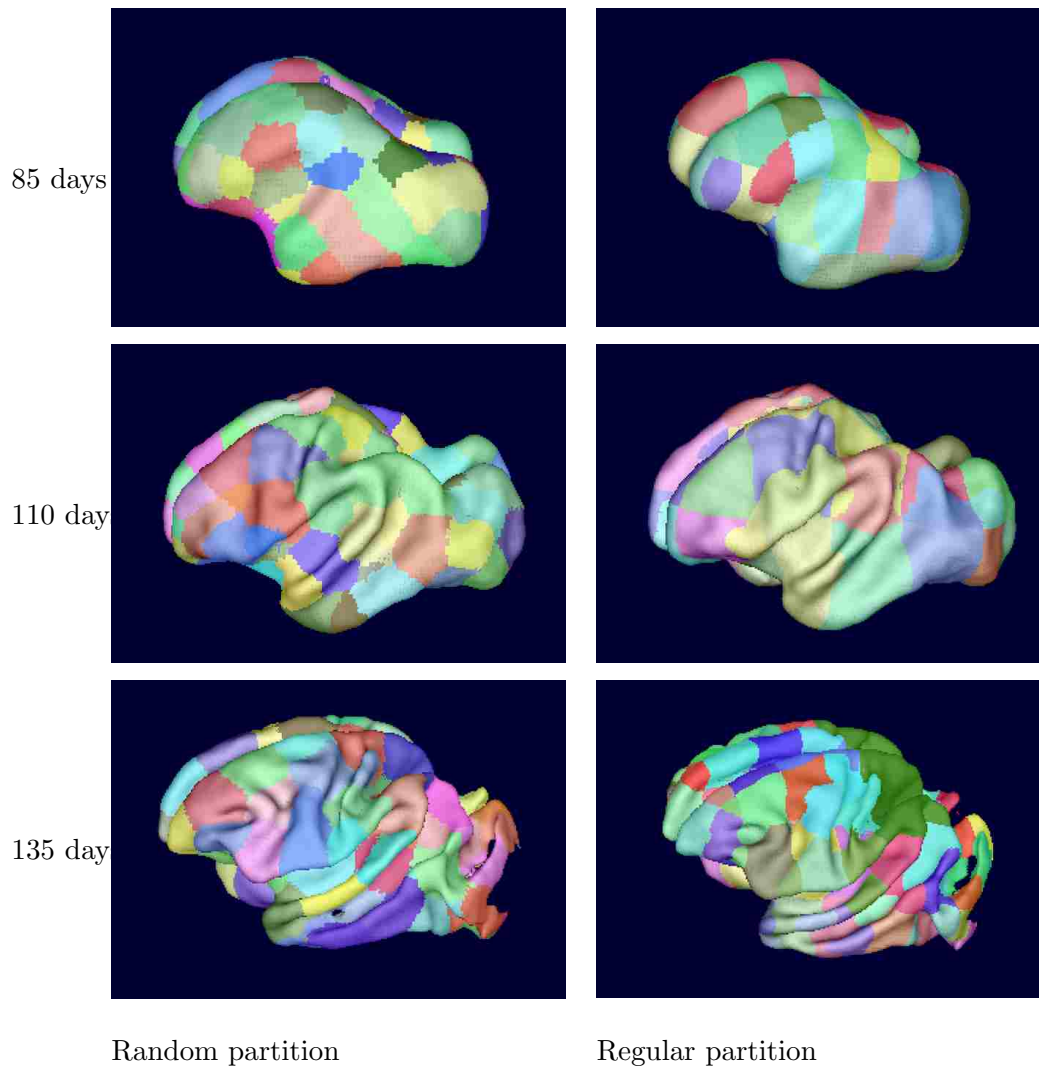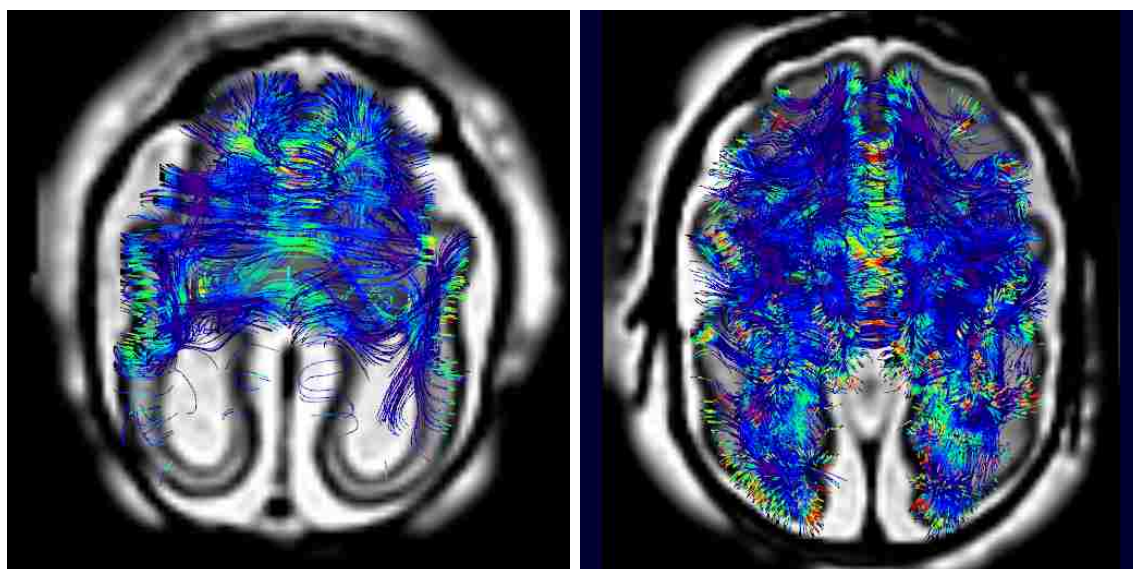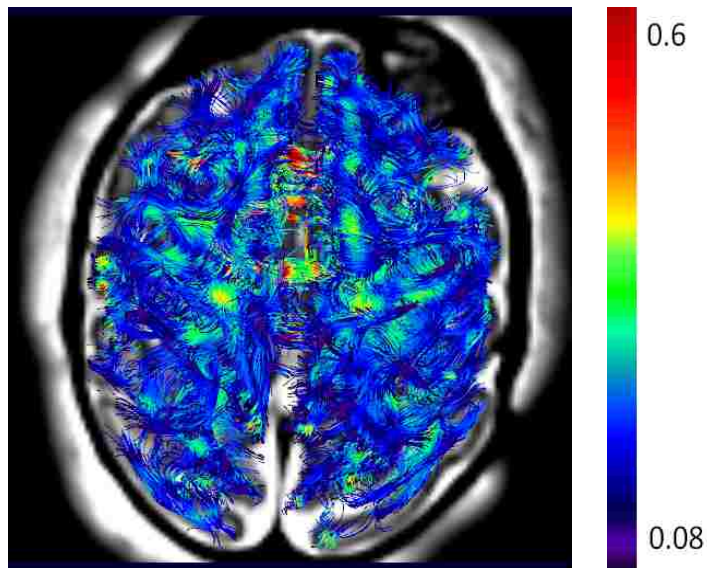Figure 5.5: 3D surface renderring of partitioned brains at all 3 time points using both random and regular parcellation schemes.

(a) 85 days

(b) 110 days

(c) 135 days

Figure 5.6: All fiber tracts connecting cortical ROI's traced at all 3 time points. The fibers are overlaid on T2W structural images and colored by FA map.

space. This enables us to obtain information more intuitively from the adjacency matrix as neighbouring indices are more likely to correspond to neighbouring ROI's. Comparing the two matrices we can see that connectivity in the brain network is more locally condensed than that of the randomized network.

Cortical connectivity

Fig. 5.8 shows the results of small-world analysis of the cortical connectivity network. We can observe that the cortical connectivity network also exhibits small-world characteristics. Besides, the cluster coefficient and global efficiency increase across brain development. These results are also robust to the number of ROI's in the experimental range.

We performed small-world analysis on the extracted graphs. From Fig. 5.7(a,b), we can see that the cluster coefficient of subcortical connectivity networks is much larger than that of the random networks while the global efficiency is slightly smaller, indicating that these networks both exhibit small-world characteristics. Both the cluster coefficient and the global efficiency increase as the brain develops. Fig. 5.7(c,d) indicates that these network properties are robust to parcellation schemes and different numbers of ROI's to partition. However, the number of ROI's should not be too small to better reveal the development of the fetal brain connectivity network, especially for global efficiency of the brain networks at 110 days and 135 days, when the brain is largest.

5.4   Conclusion and Discussion

The results of cortical and subcortical connectivity networks both identified small-world characteristics of the fetal brain network. This suggests that the characteristics of brain network have been selected to solve the problem of optimizing the brain information processing since its very early development stage. Besides, the studies also demonstrated a pattern of increased cluster coefficients as well as global efficiency, meaning the overall efficiency of the brain in processing information increases during its maturation. These observations parallel the fact that myelination is in progress and only partially formed at birth [11]. Furthermore,

Figure 5.7: Subcortical connectivity: cluster coefficient and global efficiency (mean±standard deviation) as a function of the number of nodes at all 3 ages. (a,b) compare these measurements of random partition based brain network and random network for testing the small-worldness of subcortical brain networks. (c,d) compare the measurements obtained from both random and regular partition methods.
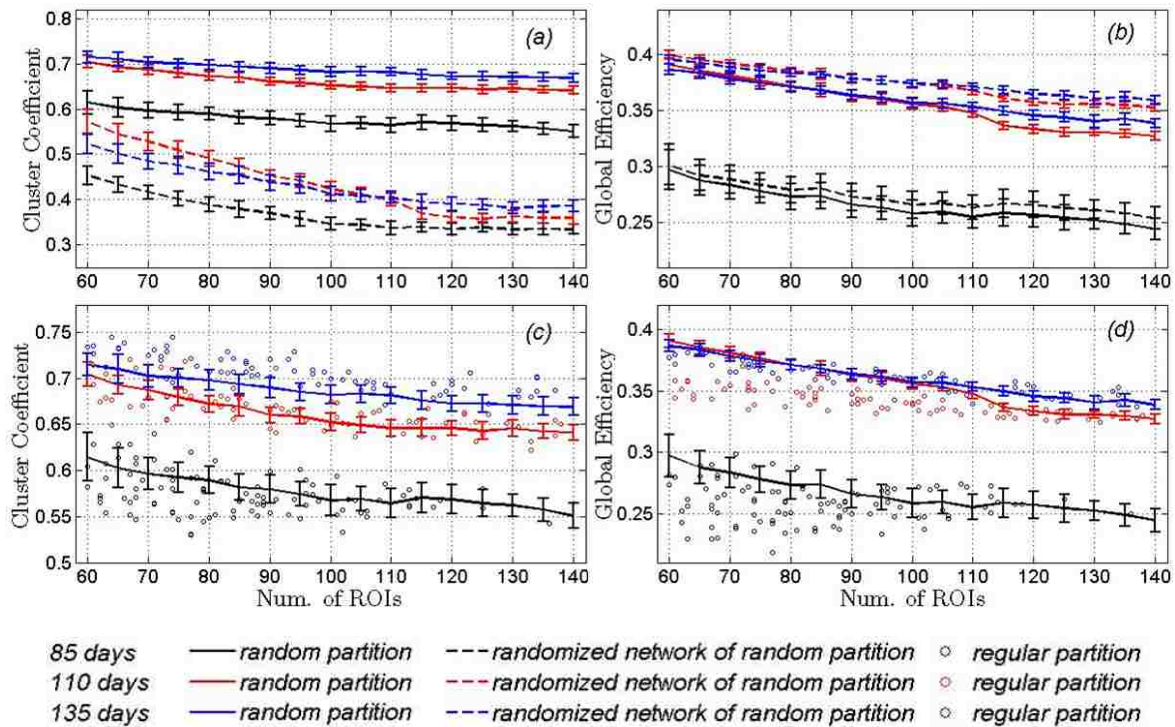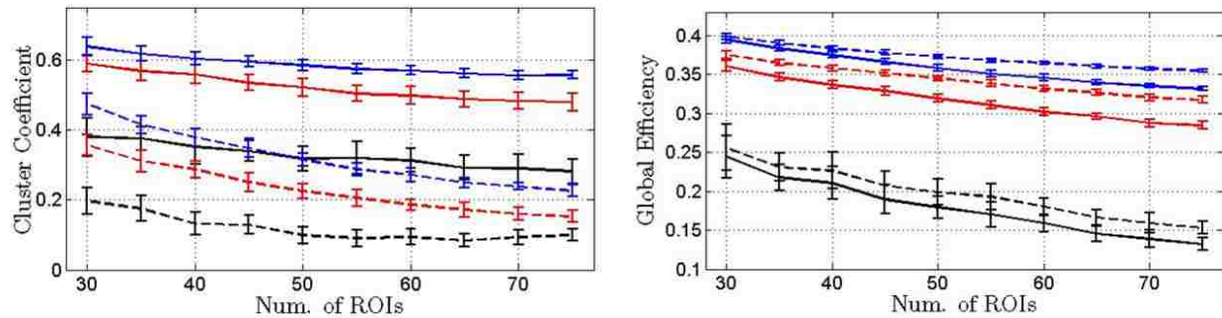
Figure 5.8: Cortical connectivity: cluster coefficient and global efficiency (mean±standard deviation) as a function of the number of nodes based on random partition scheme at all 3 ages. These measurements of random graphs are also plotted as dashed lines for testing the small-worldness of cortical brain networks. *For legend see Fig. 5.7.*

the robustness of these results to the number of ROI's indicates the feasibility of applying small-world analysis to studying developing fetal brains which is undergoing considerable size and shape changes. Another observation from the small-world analysis is that the cluster coefficients of the brain network decrease linearly as the number of ROI's increases, however the cluster coefficients of the random network seem to decrease quadratically, as shown in Fig. 5.7(a) and Fig. 5.8. This could potentially be useful in predicting abnormalities in fetal brain connectivity.

In conclusion, we have studied the changes in structural connectivity networks in the monkey fetal brain using unbiased random and regular parcellation schemes and graph theory based analysis. The findings provide a picture of the development of fetal brain networks, complementing the existing studies in adult and baby brain networks. Future work will explore the use of these measures in normal human development and their use in studying and quantifying abnormal connectivity [33].

Chapter 6

CONCLUSIONS

In chapter 1, we have briefly introduced the current research advances in fetal brain study enabled by conventional structural MRI. This motivates the technique development in DW-MRI for better complementary fetal brain study. Therefore, in the thesis we focus on addressing some key challenges in fetal DW-MRI, including ODF reconstruction from motion scattered DWI slices and the applications of DW-MRI to study fetal brain connectivity.

In chapter 2, we have discussed the diffusion process and its mathematical models, including the rank 2 tensor model and spherical harmonic model. We also discussed the diffusion property inside the brain and its application to the DW-MRI. The basic principles of DW-MRI was introduced in the end.

In chapter 3, we introduced the cause of the motion artifacts in fetal brain MRI. We then presented the current state-of-the-art methodology for slice motion estimation for DW-MRI. The motion parameters are iteratively estimated in a maximum likelihood framework, using a slice to volume registration with explicit incorporation of ST equation.

In chapter 4, we have discussed a super-resolution framework for reconstructing the ODF volume from motion scattered DWI slices. We also pointer out that this framework can also be derived from the maximum log-likelihood framework. We proposed to extend the diffusion model from rank 2 tensor model to spherical harmonic model for more complex ODF description. The experimental results have shown that the proposed extension makes it possible to accurately depict crossing fiber tracts for both adult and in-utero imaging data.

In chapter 5, we have presented the studies of changes in structural connectivity networks in the macaque fetal brain using unbiased template-free parcellation schemes and graph theory based analysis. This piece of work is a direct application of the work in chapter 3 and

chapter 4, as this can not be achieved if the image motion artifacts are not removed and the 3-D ODF volume is not reconstructed.

BIBLIOGRAPHY

[1] R. Bammer. Basic principles of diffusion-weighted imaging. *European Journal of Radiology*, 45(3):169–184, 2003.

[2] P.J. Basser and C. Pierpaoli. Microstructural and physiological features of tissues elucidated by quantitative-diffusion-tensor mri. *Journal of Magnetic Resonance*, 111:209–219, 1996.

[3] D.S. Bassett and E. Bullmore. Small-world brain networks. *The Neuroscientist*, 12(6):512–523, 2006.

[4] C. Beaulieu. The basis of anisotropic water diffusion in the nervous system - a technical review. *NMR IN BIOMEDICINE*, 15:435–455, 2002.

[5] D.L. Bihan. Diffusion mri: what water tells us about the brain. *EMBO Molecular Medicine*, 6(5):569–573, 2014.

[6] J.W. Bohland, H. Bokil, C.B. Allen, and P.P. Mitra. The brain atlas concordance problem: Quantitative comparison of anatomical parcellations. *PLoS ONE*, 4(9):1–18, 2009.

[7] E. Carmi, S. Liu, N. Alon, A. Fiat, and D. Fiat. Resolution enhancement in mri. *Magnetic Resonance Imaging*, 24(2):133–154, 2006.

[8] X. Cheng, J. Wilm, S. Seshamani, M. Fogtmann, C. Kroenke, and C. Studholme. Adapting parcellation schemes to study fetal brain connectivity in serial imaging studies. *IEEE EMBS*, pages 73–76, 2013.

[9] D.C. Van Essen and K. Ugurbil. The future of the human connectome. *NeuroImage*, 62(2):1299–1310, 2012.

[10] Y. Fan, F. Shi, J.K. Smith, W. Lin, J.H. Gilmore, and D. Shen. Brain anatomical networks in early human brain development. *NeuroImage*, 54:1862–1871, 2009.

[11] R.D. Fields. White matter matters. *Scientific American*, 298:54–61, 2008.

[12] M. Fogtmann, S. Seshamani, K. Kim, T. Chapman, and C. Studholme. A unified approach for motion-estimation and super-resolution reconstruction from structural magnetic resonance imaging on moving subjects. *MICCAI Workshop on Perinatal and Paediatric Imaging: PaPI*, pages 9–16, 2012.

[13] M. Fogtmann, S. Seshamani, C. Kroenke, X. Cheng, T. Chapman, J. Wilm, F. Rousseau, and C. Studholme. A unified approach to diffusion direction sensitive slice registration and 3-d dti reconstruction from moving fetal brain anatomy. *IEEE Transaction on Medical Imaging*, 33(2):272–289, 2014.

[14] B. Gabin. https://classes.soe.ucsc.edu/cmps160/spring13/projects/bgabin/final/ report/spherical harmonic lighting comparison.htm. 2013.

[15] J.L. Gauvain. Maximum a posteriori estimation for multivariate gaussian mixture observations of markov chains. *IEEE Transaction on Speech and Audio Processing*, 2(2):291–298, 1994.

[16] A. Gholipour, J.A. Estroff, C.E. Barnewolt, R.L. Robertson, P.E. Grant, B. Gagoski, S.K. Warfield, O. Afacan, S.A. Connolly, J.J. Neil, A. Wolfberg, and R.V. Mulkern. Fetal mri: A technical update with educational aspirations. *Concepts in Magnetic Resonance Part A*, 2015.

[17] A. Gholipour, J.A. Estroff, and S.K. Warfield. Robust super-resolution volume reconstruction from slice acquisitions: application to fetal brain mri. *IEEE Transactions on Medical Imaging*, 29(10):1739–1758, 2010.

[18] G. Gong, Y. He, L. Concha, C. Lebel, D.W. Gross, A.C. Evans, and C. Beaulieu. Mapping anatomical connectivity patterns of human cerebral cortex using in vivo diffusion tensor imaging tractography. *Cerebral Cortex Match*, 19:524–536, 2009.

[19] H. Greenspan, S. Peled, G. Oz, and N. Kiryati. Mri inter-slice reconstruction using super-resolution. *MICCAI*, 26(1):S205–23, 2001.

[20] E.M. Haacke, R.W. Brown, M.R. Thompson, and R. Venkatesan. *Magnetic Resonance Imaging: Physical Principles and Sequence Design*. John Wiley & Sons, Inc., 1999.

[21] P. Hagmann, L. Jonasson, P. Maeder, J.-P. Thiran, V.J. Wedeen, and R. Meuli. Understanding diffusion mr imaging techniques: From scalar diffusion-weighted imaging to diffusion tensor imaging and beyond. *Radiographics*, 26(1):S205–23, 2006.

[22] P. Hagmann, M. Kurant, X. Gigandet, P. Thiran, V.J. Wedeen, R. Meuli, and J.-P. Thiran. Mapping human whole-brain structural networks with diffusion MRI. *PLoS ONE*, 2(7):e597, 2007.

[23] H. Huang, R. Xue, J. Zhang, T. Ren, L.J. Richards, P. Yarowsky, M.I. Miller, and S. Mori. Anatomical characterization of human fetal brain development with diffusion tensor magnetic resonance imaging. *J. Neurosci*, 29(13):4263–4273, 2009.

[24] P.S. Huppi and J. Dubois. Diffusion tensor imaging of brain development. *Seminars in Fetal and Neonatal Medicine*, 11:489–497, 2006.

[25] M. Irani and S. Peleg. Super resolution from image sequences. *ICPR*, 2:115–120, 1990.

[26] Y. Iturria-Medina, R.C. Sotero, E.J. Canales-Rodríguez, Y. Alemán-Gómez, and L. Melie-García. Studying the human brain anatomical network via diffusion-weighted MRI and graph theory. *NeuroImage*, 40:1064–1076, 2008.

[27] S. Jiang, H. Xue, S. Counsell, M. Anjari, J. Allsop, M. Rutherford, D. Rueckert, and J. V Hajnal. Diffusion tensor imaging (dti) of the brain in moving subjects: application to in-utero fetal and ex-utero studies. *Magn. Reson. Med.*, 62(3):645–655, 2009.

[28] S. Jiang, H. Xue, A. Glover, M. Rutherford, D. Rueckert, and J.V. Hajnal. Mri of moving subjects using multislice snapshot images with volume reconstruction (svr): Application to fetal, neonatal, adult brain studies. *IEEE Trans. Med. Imag.*, 26(7):967–980, 2007.

[29] S. H. Joshi, A. Marquina, S. J. Osher, I. Dinov, J. D. Van Horn, and A. W. Toga. Mri resolution enhancement using total variation regularization. *Proc. 6th IEEE Int. Conf. Symp. Biomed. Imag.: From Nano to Macro*, pages 161–164, 2009.

[30] G. Kasprian, P. C. Brugger, M. Weber, M. Krssak, E. Krampl, C. Herold, and D. Prayer. In utero tractography of fetal white matter development. *NeuroImage*, 43(2):213–224, 2008.

[31] B. Kim, J.L. Boes, P.H. Bland, T.L. Chenevert, and C.R. Meyer. Motion correction in fmri via registration of individual slices into an anatomical volume. *Magnetic Resonance in Medicine*, 41:964–972, 1999.

[32] K. Kim, P.A. Habas, F. Rousseau, O.A. Glenn, A.J. Barkovich, and C. Studholme. Intersection based motion correction of multislice mri for 3-d in utero fetal brain image formation. *IEEE Transactions on Medical Imaging*, 29(1):146–158, 2010.

[33] M. Koob, A.-S. Weingertner, B. Gasser, E. Oubel, and J.-L. Dietemann. Thick corpus callosum: a clue to the diagnosis of fetal septopreoptic holoprosencephaly? *Pediatr Radiol*, 42(7):886–890, 2011.

[34] D.C. Liu and J. Nocedal. On the limited memory bfgs method for large scale optimization. *Math. Program.*, 45(3):503–528, 1989.

[35] S. Mori and P.C.M. van Zijl. Fiber tracking: principles and strategies - a technical review. *NMI IN BIOMEDICINE*, 15:468–480, 2002.

[36] S. Mori and J. Zhang. Principles of diffusion tensor imaging and its applications to basic neuroscience research. *Neuron*, 51(5).

[37] E. Oubel, M. Koob, C. Studholme, J.-L. Dietemannn, and F. Rousseau. Reconstruction of scattered data in fetal diffusion mri. In *MICCAI*, pages 574–581, 2010.

[38] H. Park, C.R. Meyer, and B. Kim. Improved motion correction in fmri by joint mapping of slices into an anatomical volume. *MICCAI*, 3217:745–751, 2004.

[39] R.R. Peeters, P. Kornprobst, M. Nikolova, S. Sunaert, T. Vieville, G. Malandain, R. Deriche, O. Faugeras, M. Ng, and P.V. Hecke. The use of super-resolution techniques to reduce slice thickness in functional mri. *International Journal of Imaging Systems and Technology*, 2208:1204–1206, 2004.

[40] J. Philibert. One and a half century of diffusion: Fick, einstein, before and beyond. *Diffusion Fundamentals*, 2:1.1–1.10, 2005.

[41] F. Rousseau, O.A. Glenn, B. Iordanova, C. Rodriguez-Carranza, D.B. Vigneron, J.A. Barkovich, and C. Studholme. Registration-based approach for reconstruction of high-resolution in utero fetal mri brain images. *Acad Rad*, 13:1072–1081, 2006.

[42] F. Rousseau, K. Kim, C. Studholme, M. Koob, and J. Dietemann. On super-resolution for fetal brain mri. In *MICCAI*, pages 55–362, 2010.

[43] M. Rubinov and O. Sporns. Complex network measures of brain connectivity: Uses and interpretations. *NeuroImage*, 52:1059–1069, 2010.

[44] B. Scherrer, A. Gholipour, and S.K. Warfield. Super-resolution in diffusion-weighted imaging. In *MICCAI*, pages 124–132, 2011.

[45] T. Schultz, C.-F. Westin, and G. Kindlmann. Multi-diffusion-tensor fitting via spherical deconvolution: A unifying framework. In *MICCAI*, pages 674–681, 2010.

[46] S. Seshamani, M. Fogtmann, X. Cheng, M. Thomason, Gatenby C, and C. Studholme. Cascaded slice to volume registration for moving fetal fmri. *Biomedical Imaging (ISBI), 2013 IEEE 10th International Symposium on*, pages 796–799, 2013.

[47] E.O. Stejskal and J.E. Tanner. Spin diffusion measurements: spin echoes in the presence of a time-dependent field gradient. *J Chem Phys*, 42:288–292, 1965.

[48] C. Studholme. Mapping fetal brain development in utero using magnetic resonance imaging: The big bang of brain mapping. *Ann. Rev. Bio. Eng.*, 13(1):345–368, 2011.

[49] C. Studholme. Mapping the developing human brain in utero using quantitative mr imaging techniques. *Seminars in Perinatology*, 39(2):105–112, 2015.

[50] C. Studholme and F. Rousseau. Quantifying and modelling tissue maturation in the living human fetal brain. *International Journal of Developmental Neuroscience*, 32:3–10, 2014.

[51] A. Tikhonov. Regularization of incorrectly posed problems. *Sov. Math. Dokl.*, 4:1624–1627, 1963.

[52] J.-D. Tournier, F. Calamante, and A. Connelly. Robust determination of the fibre orientation distribution in diffusion mri: non-negativity constrained super-resolved spherical deconvolution. *NeuroImage*, 35:674–681, 2007.

[53] R.Y. Tsai and T.S. Huang. Multiframe image restoration and registration. *in Advances in Computer Vision and Image Processing*, 1(7):317–339, 1984.

[54] O. Tymofiyeva1, C.P. Hess, E. Ziv, N. Tian, S.L. Bonifacio, P.S. McQuillen, D.M. Ferriero, A.J. Barkovich1, and D. Xu. Baby connectome: Mapping the structural connectivity of the newborn brain. *NeuroImage*, 52:1059–1069, 2010.

[55] J. Wang, L. Wang, Y. Zang, H. Yang, H. Tang, Q. Gong, Z. Chen, C. Zhu, and Y. He. Parcelation-dependent small-world brain functional networks: A resting-state fmri study. *Human Brain Mapping*, 30(5):1511–1523, 2009.

[56] J. Wilm. Analysis of diffusion tensor imaging of in-utero fetal monkey brains. Master's thesis, Technical University of Denmark, Denmark, 2012.

[57] E. Zanin, J.-P. Ranjeva, S. Confort-Gouny, M. Guye, D. Denis, P.J. Cozzone, and N. Girard. White matter maturation of normal human fetal brain. an in vivo diffusion tensor tractography study. *Brain Behav.*, 1(2):95–108, 2011.